Albert-Ludwigs-Universität Freiburg

Bachelor Thesis

Analysis of the Tunnel Effect for a Quantum Walker

Author:
Luisa Robin Grether

Supervisor:
Prof. Dr. Andreas Buchleitner

In cooperation with:
Dr. Felix Thiel

A thesis submitted in partial fulfillment of the requirements for the degree

Bachelor of Science

Fakultät für Mathematik und Physik
Physikalisches Institut
Quantum Optics and Statistics
August 17, 2020 – reprinted April 3, 2026

Abstract

The following thesis studies the tunnel effect for a continuous-time quantum walker using a stroboscopic measurement protocol. For this, we consider the tight-binding Hamiltonian on a one-dimensional infinite lattice with coupling strength γ, and additionally introduce a rectangular barrier of thickness d and height ε. We then regard a particle initially located at x_i on the left side of the barrier, which evolves freely according to the corresponding Schrödinger equation; but at discrete times $t = n\tau, n \in \mathbb{N}$, we implement projective measurements at the pre-defined detection site x_d on the right side of the barrier. Within this setup, we ask for the probability F_n that the first successful detection at x_d occurs at the nth measurement attempt. The Hamiltonian is diagonalized and we find a continuous energy band $-2\gamma \leq E \leq 2\gamma$ with up to d additional discrete eigenvalues $E > 2\gamma$ depending on the barrier height ε. Using the method of steepest descents, we derive an asymptotic expansion for the transition amplitude $\langle x_d|U(t)|x_i\rangle$ and the return amplitude $\langle x_d|U(t)|x_d\rangle$ for $t \to \infty$. From these amplitudes, the probability F_n is calculated using a quantum renewal equation. By numerical simulation, we find that $F_n \propto n^{-3}$ similar to the case without barrier. Furthermore, the Hartman effect is recovered in the position of the maximum of F_n and in the mean first detection time $\langle T\rangle$. Lastly, we present an ansatz to analytically calculate F_n from the amplitudes $\langle x_d|U(t)|x_i\rangle$ and $\langle x_d|U(t)|x_d\rangle$.

In der nachfolgenden Arbeit wird der Tunneleffekt für einen Quantum Walker unter stroboskopischen Messungen untersucht. Hierfür betrachten wir den Tight-Binding Hamiltonian mit Kopplungsstärke γ auf einem eindimensionalen, unendlichen Gitter und führen zusätzlich eine rechteckige Potentialbarriere der Breite d und Höhe ε ein. Nun betrachten wir ein Teilchen, dass sich zu Beginn bei x_i links von der Barriere befindet. Dieses bewege sich zunächst frei gemäß der Schrödinger-Gleichung, jedoch führen wir zu festen Zeitpunkten $t = n\tau, n \in \mathbb{N}$ projektive Messungen am zuvor definierten Detektionsort x_d auf der rechten Seite der Barriere durch. Gesucht ist nun die Wahrscheinlichkeit F_n, dass der $n$te Messversuch die allererste erfolgreiche Detektion des Teilchens bei x_d liefert. Wir diagonalisieren den zugrundeliegenden Hamiltonian und finden heraus, dass dieser aus einem kontinuierlichen Energieband $-2\gamma \leq E \leq 2\gamma$ und bis zu d zusätzlichen, diskreten Energiezuständen mit $E > 2\gamma$, abhängig von der Barrierenhöhe ε, besteht. Mittels der Sattelpunktsmethode bestimmen wir eine asymptotische Entwicklung für die Übergangsamplitude $\langle x_d|U(t)|x_i\rangle$ und die Rückkehramplitude $\langle x_d|U(t)|x_d\rangle$ im Grenzfall $t \to \infty$. Durch eine Erneuerungsgleichung berechnen wir aus diesen Amplituden die Verteilung F_n. Mit einer numerischen Simulation finden wir heraus, dass $F_n \propto n^{-3}$ analog zum Fall ohne Potentialbarriere. Des Weiteren finden wir den Hartman-Effekt in der Position des Maximums von F_n und in der mittleren Erst-Detektions-Zeit $\langle T\rangle$ wieder. Zuletzt zeigen wir einen Ansatz, um F_n aus den Amplituden $\langle x_d|U(t)|x_i\rangle$ und $\langle x_d|U(t)|x_d\rangle$ analytisch zu bestimmen.

Acknowledgements

First, I would like to thank my supervisor *Andreas Buchleitner*. About one year ago, I visited your lecture and you taught me the theoretical foundations of quantum mechanics. Your mathematically rigorous course, the interesting examples from quantum information theory and not least the ice cream you treated me, after I had passed the exam, motivated me to join your research group for my Bachelor thesis. Thank you very much for your support and for enabling me to be part of your working group.

Next, I want to thank *Edoardo Carnio* and *Gabriel Dufour*, who introduced me to the key topics that the research group is currently working on, and thereby also contributed to my decision to join the group. Furthermore, I thank *Fabian Spallek* for his useful advice and for being my first contact person in the office.

But my biggest thanks go to *Felix Thiel*. You arouse my interest in the topic of this thesis. You guided me through the planning and implementation of this work. Thank you for your valuable advice, your comprehensive explanations and our useful discussions. Without your support in every step throughout my thesis, this project would have never been accomplished.

Contents

List of Figures

Chapter 1

Introduction

1.1 Quantum tunneling

Since the development of quantum mechanics in the first half of the 20th century, the phenomenon of quantum tunneling has constantly been of great interest. Although a similar phenomenon, namely frustrated total internal reflection, had been known for decades already back then [1]; tunneling impressed the physicists because it was one of the major new concepts which quantum mechanics introduced in contrast to classical mechanics. And because of its inconsistency with our everyday experience, this fascination continues until today. On the other hand, quantum tunneling is interesting because it is crucial for many microscopic and macroscopic processes such as α-decay [2] and hydrogen fusion inside the sun. And moreover, because of the advances in the semiconductor technology within the past decades, it plays an increasingly important role in engineering as well.

The main question of quantum tunneling, how likely it is that a particle penetrates a given barrier, is quite easy to solve in many circumstances. On the contrary, the issue of how much time a particle needs to do so remains controversial until today. This question eventually comes down to two conceptional issues. First, it has been shown that the Schrödinger formalism does not allow the existence of a time-of-arrival operator [3]. Moreover, a quantum particle does not have a trajectory; one can only know its position and momentum by measurement (and only up to a limited finite precision). The measuring process, however, inevitably alters the particle's behavior. As a consequence, there cannot be an intrinsic definition of a transmission time corresponding to what is known in classical mechanics. Nevertheless, a lot of effort has been put into finding a way of measuring the tunneling time.

A very prominent ansatz is the so-called Wigner time delay [4, 5]. Consider a wave packet which is peaked around a single wave vector k (e.g. a Gaussian wave packet). If we follow the wave packet while it penetrates a barrier, we find that its peak experiences a time delay in comparison to the peak of a freely evolving wave packet. This delay is (in the stationary phase approximation) given by the energy derivative of the phase shift that the wave function experiences upon transmission. The main problem with this ansatz is that the wave packet may be significantly distorted by the transmission because the barrier acts as a high-pass filter. Therefore, it may be questionable whether the relation between the peak of the incoming undistorted packet and the peak of the transmitted altered packet provides useful information about the time spent underneath the barrier.

Other approaches introduce additional degrees of freedom to mimic a clock [6]: E.g. in the Larmor clock approach, a spin is assigned to the particle and a magnetic field is applied in the barrier region. As a result, one can determine the time which the particle spent underneath the barrier by measuring its Larmor precession. However, the problem with additional degrees of freedom is that they can interfere with the original tunnel effect. Thereby, the resulting tunneling time may only be valid for the specific considered clock approach and may, correspondingly, not provide any information about the tunnel effect without additional degrees of freedom.

A third group of approaches is based on alternative formulations of quantum mechanics [7]: E.g. the Feynman path integral approach assigns a distinct tunneling time to every possible 'trajectory' that the particle can follow [8]. However, the main problem with these alternative formulations is that the obtained tunneling times are in general complex-valued and it is not intrinsically clear how these should be interpreted in comparison to real times that one expects from an experiment.

While there are many more ansatzes as well [9], many of them share one very interesting consequence: The predicted transmission time of a tunneling particle is independent of the barrier thickness and even shorter than the time a particle would need to travel the same distance if there were no barrier at all. This phenomenon was intensively studied by Hartman in 1962 [10] and eventually called the Hartman effect. Under certain conditions, it even predicts a superluminal propagation for the tunneling particle, which is why the effect attracted great attention in the past. An interpretation for this effect is that the tunneling process is mediated by non-local virtual particles violating special relativity [11]. This interpretation is, however, highly controversial. A different explanation ansatz is as follows: The transmission coefficient of a potential barrier usually increases with increasing momentum of the incoming particle, i.e. the barrier acts as a high-pass filter. Consequently, the transmitted part of the particle's wave function has a higher average momentum than the original wave before the scattering process. As a result, it looks as if the particle had gathered additional momentum by penetrating the barrier, which explains the faster propagation.

In contrast to the many different theoretical definitions, only few experiments concerning the tunneling time were conducted before the 2000s. In 1993, the authors of [12] measured the tunneling time of single photons in agreement with the Wigner time delay. Through the development of ultrafast lasers and attosecond metrology, more experiments have been implemented in the past two decades especially using strong laser field ionization; however, yielding inconsistent results: While e.g. the authors of [13] claim to have found "an upper limit of 1.8 attoseconds on any tunneling delay", contradictory to all common definitions of the tunneling time, the authors of [14] measured a finite delay time that, within their experimental error, is reported to be compatible only with the Larmor clock time and with the tunneling time according to the path integral formulation.

In summary, the issue of the tunneling time remains unresolved; though most controversy about it eventually comes down to the problem that there exists only an operational definition for it. Moreover, many ansatzes to define the tunneling time (except e.g. the clock approaches) do not incorporate any actual measurement procedures; so it remains unclear how corresponding experiments should be implemented. In contrast, we will precisely define the measurement process in our study of quantum tunneling. For this, we base our examination on the formalism of the quantum walk and implement a stroboscopic measurement protocol, which are both introduced in the

next sections.

1.2 Quantum walks

For more than one century, the theory of random walks has been well studied. Through advances in theoretical quantum computation and experimental trapping of single atoms within the last two decades, its quantum analogue, the so-called quantum walk, has obtained much attention.

The quantum walk was first introduced in 1993 by Aharonov, Davidovich and Zagury [15] (originally under the name 'quantum random walk') by considering a quantum particle on a lattice. This particle is assigned an additional internal degree of freedom which is changed periodically to resemble a classical coin flip and the particle as a whole is moved on the lattice according to the current value of the internal degree of freedom. Since this approach considers discrete time steps only, it is called the discrete-time quantum walk.

A different ansatz was established in 1998 by Farhi and Gutmann [16]. Within developing a quantum algorithm to solve decision problems, they introduced the continuous-time quantum walk. This approach considers the propagation of a quantum particle on an arbitrary lattice in the tight-binding approximation, which originated from solid-state physics.

While the classical random walk is a pretty slow process, in the sense that the mean squared displacement grows only linearly in time (i.e. diffusive spreading) [17, p. 43], both approaches to the quantum walk yield a mean squared displacement which grows quadratically in time (i.e. ballistic spreading), and which has been verified experimentally [18, 19].

Now, consider a random walker initially located at some position x_i. How long does it take until the walker arrives for the first at some other place $x_d \neq x_i$ averaged over all possible trajectories? The answer to this question is called the mean first arrival time; and in 1915 already, Schrödinger showed that, because of the diffusive motion, its value diverges for the random walk [20]. On the contrary, for the quantum walker with ballistic motion, one would at first expect a finite mean first arrival time. However, if we attempt to properly define it, we come back to the two issues discussed in the previous section: There exists no time-of-arrival operator in the quantum formalism [3]; and further, the quantum walker does not have a definite trajectory. Hence, there really exists no canonical analogue of the mean first arrival time in the quantum case.

Nevertheless, the issue of when a quantum walker will arrive for the first time at some pre-defined destination is very relevant for quantum computing because "it is closely related to the quantum search problem and translates to the question of when [such] a [quantum] computation result becomes available" [21]. With this in mind, it is high time for this issue to be solved considering the great efforts put into the development of quantum computers, which fundamentally rely on robust and well-studied quantum algorithms.

In this thesis, we analyze the tunnel effect as it appears to a continuous-time quantum walker. As usual, we implement the quantum walk within the formalism of the tight-binding approximation, which gives two advantages compared to a continuous position space. First, it simplifies both theoretical definition and experimental implementation of measurement processes because we deal with a wave function that can be localized at pre-defined lattice sites only. Second, it corresponds more directly to

applications in quantum search algorithms which usually deal with graphs.[1] Additionally, we introduce a potential barrier. For brevity, we will only consider the simplest case in the following analysis, i.e. an infinite one-dimensional lattice and a rectangular potential barrier. The exact realization of this barrier is defined in Chapter 2.

1.3 Stroboscopic measurement protocol

To overcome the lack of a first arrival time definition, we follow the authors of [22, 23, 24] whose central idea is the introduction of a series of stroboscopic measurements. Consider a particle that is initially located at some lattice site x_i. Now, we let this particle evolve freely according to the tight-binding Hamiltonian (with an additional potential barrier in our case); but at discrete times $t \in \{\tau, 2\tau, ...\}$, we make projective measurements at a pre-defined detection site x_d. Hereby, we use the standard von Neumann projective measurement, which implies the projection of the particle's state vector on $|x_d\rangle$ and subsequent renormalization [25]. To study the tunnel effect, we choose x_i and x_d on opposite sides of the barrier. Then, instead of asking when the particle will arrive at x_d (which remains undefined), we ask for the probability F_n that the *first successful detection* at x_d will occur at time $t = n\tau$ ($n \in \mathbb{N}^+$).

Using this ansatz, we finally deal with a clearly defined measurement problem instead of the insufficiently defined arrival problem. However, this approach also incorporates two disadvantages. First, it limits our analysis' results to a discrete time space $t = n\tau, n \in \mathbb{N}^+$; and second, the projective measurements have a critical impact on the dynamics of the system. In particular, the time evolution including these projective measurements is not unitary anymore, which makes the computation harder. The authors of [23], however, showed that the so-called first detection amplitude φ_n, with $F_n = |\varphi_n|^2$, obeys a renewal equation[2]

$$\varphi_n = \langle x_d|U(n\tau)|x_i\rangle - \sum_{j=1}^{n-1} \varphi_j \langle x_d|U((n-j)\tau)|x_d\rangle \,, \tag{1.1}$$

where $U(t) = \mathrm{e}^{-\mathrm{i}\mathcal{H}t/\hbar}$ and $\mathcal{H}$ are the unitary evolution operator and Hamiltonian of the original system without measurements, respectively. Eq. (1.1) enables a simple calculation of φ_n and F_n via the unitary dynamics of the unperturbed system and will be the central tool in this thesis.

Outline

Incorporating this approach, we start our analysis in Chapter 2 with a precise definition of the Hamiltonian and the potential barrier. Then, we solve the corresponding time-independent Schrödinger equation to find the energy eigenstates as well as the transmission and reflection coefficient of our barrier. At the end of the chapter, the results will be verified by a finite-size numerical simulation. In the following Chapter 3, we use the energy representation of the system to determine its unitary dynamics. In

[1] A lattice in the tight-binding approximation is nothing other than an unweighted and undirected graph.

[2] In probability theory, a 'renewal equation' relates the momentary value of the variable of a stochastic process to all the values it took on before.

particular, we derive an asymptotic expansion for $t \to \infty$ of the transition amplitude $\langle x_d|U(t)|x_i\rangle$ and of the return amplitude $\langle x_d|U(t)|x_d\rangle$, which both appear in the renewal equation (1.1). Our analytic results are again compared to numerical simulation. Then, in Chapter 4, we numerically analyze the first detection probability F_n. In particular, we investigate the asymptotic behavior of F_n for $n \to \infty$, and analyze its characteristic attributes, i.e. the global maximum and the mean first detection time $\langle T\rangle$. Lastly, we present an ansatz to analytically calculate F_n from the amplitudes $\langle x_d|U(t)|x_i\rangle$ and $\langle x_d|U(t)|x_d\rangle$. Finally, the thesis is closed with a discussion and summary in Chapter 5.

Chapter 2

Energy eigenstates

2.1 Definitions and ansatz

As mentioned in the introduction, we use the tight-binding model to analyze the tunnel effect on the infinite discrete line. The lattice sites are labeled by positions $x \in \mathbb{Z}$ along the line and $|x\rangle$ denotes the associated position eigenstates, which are by definition orthogonal, i.e. $\langle y|x\rangle = \delta_{yx}$ (where δ_{yx} denotes Kronecker's delta). Using this notation, the basic Hamiltonian $\mathcal{H}_0$ is given by

$$\mathcal{H}_0 = -\gamma \sum_{x=-\infty}^{\infty} \left(|x\rangle\langle x+1| + |x+1\rangle\langle x|\right). \tag{2.1}$$

The constant $\gamma > 0$ thereby denotes the tight-binding coupling strength and fixes the energy scale, such that all energies will henceforth be measured in units of γ and all times in units of $\hbar/\gamma$. Additionally, we introduce a rectangular barrier potential of energy ε. This barrier is realized by adding $\varepsilon > 0$ to the diagonal elements of $\mathcal{H}$ at d neighboring lattice sites $0 \leq x \leq d-1$. The total Hamiltonian to be studied is therefore

$$\mathcal{H} = -\gamma \sum_{x=-\infty}^{\infty} \left(|x\rangle\langle x+1| + |x+1\rangle\langle x|\right) + \varepsilon \sum_{x=0}^{d-1} |x\rangle\langle x|. \tag{2.2}$$

To solve the time-independent Schrödinger equation $\mathcal{H}|\psi\rangle = E|\psi\rangle$, we divide the infinite line into three sectors: I: $x \leq -1$ (left side of the barrier), II: $0 \leq x \leq d-1$ (inside the barrier), III: $x \geq d$ (right side of the barrier); and use the stationary wave ansatz according to [26, pp. 13.3-13.6] with different wave vectors k for each section:

$$\langle x|\psi\rangle = \psi(x) = \begin{cases} a_1(k_\mathrm{I})\,\mathrm{e}^{\mathrm{i}k_\mathrm{I}x} + a_2(k_\mathrm{I})\,\mathrm{e}^{-\mathrm{i}k_\mathrm{I}x} & x \leq -1 \\ a_3(k_\mathrm{II})\,\mathrm{e}^{\mathrm{i}k_\mathrm{II}x} + a_4(k_\mathrm{II})\,\mathrm{e}^{-\mathrm{i}k_\mathrm{II}x} & 0 \leq x \leq d-1 \\ a_5(k_\mathrm{III})\,\mathrm{e}^{\mathrm{i}k_\mathrm{III}x} + a_6(k_\mathrm{III})\,\mathrm{e}^{-\mathrm{i}k_\mathrm{III}x} & x \geq d \end{cases}$$

When we first insert this ansatz at $x \leq -2$, at $1 \leq x \leq d-2$ and at $x \geq d+1$ into the Schrödinger equation, the coefficients $a_i(k_j)$ and the exponential factors $\mathrm{e}^{\pm\mathrm{i}k_j x}$ cancel out and yield the dispersion relation for each section:

$$E = -2\gamma\cos(k_\mathrm{I}) = \varepsilon - 2\gamma\cos(k_\mathrm{II}) = -2\gamma\cos(k_\mathrm{III})$$

We immediately see that $k_{\mathrm{III}} = k_{\mathrm{I}} + 2n\pi, n \in \mathbb{Z}$. Since our ansatz is 2π-periodic in k, we can set $k := k_{\mathrm{I}} = k_{\mathrm{III}}$ without loss of generality. Furthermore, we will use the notation $k' := k_{\mathrm{II}}$ from here on. The stationary wave ansatz now reads

$$\langle x|\psi_k\rangle = \psi_k(x) = \begin{cases} a_1(k)\,\mathrm{e}^{\mathrm{i}kx} + a_2(k)\,\mathrm{e}^{-\mathrm{i}kx} & x \leq -1 \\ a_3(k')\,\mathrm{e}^{\mathrm{i}k'x} + a_4(k')\,\mathrm{e}^{-\mathrm{i}k'x} & 0 \leq x \leq d-1 \\ a_5(k)\,\mathrm{e}^{\mathrm{i}kx} + a_6(k)\,\mathrm{e}^{-\mathrm{i}kx} & x \geq d \end{cases} \tag{2.3}$$

and the shortened dispersion relation is

$$E(k) = -2\gamma\cos(k) = \varepsilon - 2\gamma\cos(k'). \tag{2.4}$$

Since $\cos(x + \mathrm{i}y) = \cos(x)\cosh(y) - \mathrm{i}\sin(x)\sinh(y)$ [27, p. 74], we see from the dispersion relation that there exist three types of energy eigenstates which belong to a real energy $E \in \mathbb{R}$:

1. Ordinary propagation: $k \in \mathbb{R}, \quad k' \in \mathbb{R}$
2. Quantum tunneling: $k \in \mathbb{R}, \quad k' \notin \mathbb{R}$
3. Resonance states: $k \notin \mathbb{R}$

As obvious from Eq. (2.4), the eigenstates type 1 and 2 lie within the energy band $-2\gamma \leq E \leq 2\gamma$; thus, we also call them band states. The type 3 states, on the contrary, are only allowed for specific discrete values of k, k'; we call them resonance states. Before we focus on these individual eigenstates, however, we must consider also the Schrödinger equation at positions $x \in \{-1, 0, d-1, d\}$. These four equations are not trivial to solve because they relate the coefficients $a_i(k)$ to each other and thus serve as a kind of continuity condition:

$$\begin{aligned} E(k)\ \psi_k(-1) &= -\gamma\left(\psi_k(-2) + \psi_k(0)\right) \\ (E(k) - \varepsilon)\ \psi_k(0) &= -\gamma\left(\psi_k(-1) + \psi_k(1)\right) \\ (E(k) - \varepsilon)\ \psi_k(d-1) &= -\gamma\left(\psi_k(d-2) + \psi_k(d)\right) \\ E(k)\ \psi_k(d) &= -\gamma\left(\psi_k(d-1) + \psi_k(d+1)\right) \end{aligned} \tag{2.5}$$

In Sec. 2.2, we will study the eigenstates of type 1 and 2. The eigenstates of type 3 are examined in Sec. 2.3.

2.2 Eigenstates type 1 and 2 - band states

In this section, we analyze the energy eigenstates defined by Eq. (2.3) where $k \in \mathbb{R}$. According to Eq. (2.4), the energy of these band states lies in the energy band $-2\gamma \leq E(k) \leq 2\gamma$. Since the stationary wave ansatz (and thus also the dispersion relation) is 2π-periodic, we can set $k \in [0, 2\pi)$ with no loss of generality. As mentioned earlier, these eigenstates can be split into two groups. If the wave vector k' inside of the barrier region is real, we say the eigenstate is of type 1. In this case, we find an ordinary (i.e. oscillatory/sinusoidal) propagation of the wave function in all three sections of the infinite line. In contrast to this, eigenstates with $k' \notin \mathbb{R}$ feature an exponentially decaying wave function in the barrier region, i.e. quantum tunneling. We refer to these states as type 2.

To find the position space representation $\psi_k(x)$ of each energy eigenstate, we must solve the continuity conditions (2.5) to get the coefficients $a_i(k)$. However, these are only four conditions; so even if we require the states to be normalized, we have a system of merely five equations for six variables, which implies that the band states are degenerate. This issue is resolved by separately considering waves that come in from either side of the barrier. For waves coming in from the left side (i.e. negative x), we set $a_6(k) = 0$ and use $a_1(k) = a^{\mathrm{L}}$ as normalization parameter. With this ansatz, we can uniquely calculate the remaining coefficients $a_2(k), ..., a_5(k)$. In particular, we are interested in the ratios $T^{\mathrm{L}}(k) := \frac{a_5(k)}{a_1(k)}, R^{\mathrm{L}}(k) := \frac{a_2(k)}{a_1(k)}$, which define the transmission and reflection coefficient [25] ('L' indicates that the wave is coming in from the left side). Using Eq. (2.4) to express $E(k)$ through the wave vectors k and k', the results are:

$$T^{\mathrm{L}}(k) = \frac{\sin(k)\sin(k')\,\mathrm{e}^{-\mathrm{i}kd}}{\cos(dk')\sin(k)\sin(k') + \mathrm{i}\sin(dk')\,(\cos(k)\cos(k') - 1)} \tag{2.6}$$

$$R^{\mathrm{L}}(k) = -\mathrm{i}\,\frac{\frac{\varepsilon}{2\gamma}\sin(dk')\,\mathrm{e}^{-\mathrm{i}k}}{\cos(dk')\sin(k)\sin(k') + \mathrm{i}\sin(dk')\,(\cos(k)\cos(k') - 1)} \tag{2.7}$$

$$a_3(k) = a^{\mathrm{L}}\,\frac{\sin(k)\sin\left(\frac{k+k'}{2}\right)\mathrm{e}^{-\mathrm{i}(k-k'+2dk')/2}}{\cos(dk')\sin(k)\sin(k') + \mathrm{i}\sin(dk')\,(\cos(k)\cos(k') - 1)}$$

$$a_4(k) = -a^{\mathrm{L}}\,\frac{\sin(k)\sin\left(\frac{k-k'}{2}\right)\mathrm{e}^{-\mathrm{i}(k+k'-2dk')/2}}{\cos(dk')\sin(k)\sin(k') + \mathrm{i}\sin(dk')\,(\cos(k)\cos(k') - 1)}$$

and the corresponding energy eigenstates are:

$$\langle x|\psi_k^{\mathrm{L}}\rangle = \psi_k^{\mathrm{L}}(x) = \begin{cases} a^{\mathrm{L}}\left(\mathrm{e}^{\mathrm{i}kx} + R^{\mathrm{L}}(k)\,\mathrm{e}^{-\mathrm{i}kx}\right) & x \le -1 \\ a_3(k)\,\mathrm{e}^{\mathrm{i}k'x} + a_4(k)\,\mathrm{e}^{-\mathrm{i}k'x} & 0 \le x \le d-1 \\ a^{\mathrm{L}}\,T^{\mathrm{L}}(k)\,\mathrm{e}^{\mathrm{i}kx} & x \ge d \end{cases} \tag{2.8}$$

Analogously, we set $a_1(k) = 0$ and $a_6(k) = a^{\mathrm{R}}$ for waves coming in from the right side and define the ratios $T^{\mathrm{R}}(k) := \frac{a_2(k)}{a_6(k)}, R^{\mathrm{R}}(k) := \frac{a_5(k)}{a_6(k)}$ for the transmission and reflection coefficient. Again expressing everything in terms of k and k', we get:

$$T^{\mathrm{R}}(k) = \frac{\sin(k)\sin(k')\,\mathrm{e}^{-\mathrm{i}kd}}{\cos(dk')\sin(k)\sin(k') + \mathrm{i}\sin(dk')\,(\cos(k)\cos(k') - 1)} \tag{2.9}$$

$$R^{\mathrm{R}}(k) = -\mathrm{i}\,\frac{\frac{\varepsilon}{2\gamma}\sin(dk')\,\mathrm{e}^{-\mathrm{i}(2d-1)k}}{\cos(dk')\sin(k)\sin(k') + \mathrm{i}\sin(dk')\,(\cos(k)\cos(k') - 1)} \tag{2.10}$$

$$a_3(k) = -a^{\mathrm{R}}\,\frac{\sin(k)\sin\left(\frac{k-k'}{2}\right)\mathrm{e}^{\mathrm{i}(k+k'-2dk)/2}}{\cos(dk')\sin(k)\sin(k') + \mathrm{i}\sin(dk')\,(\cos(k)\cos(k') - 1)}$$

$$a_4(k) = a^{\mathrm{R}}\,\frac{\sin(k)\sin\left(\frac{k+k'}{2}\right)\mathrm{e}^{\mathrm{i}(k-k'-2dk)/2}}{\cos(dk')\sin(k)\sin(k') + \mathrm{i}\sin(dk')\,(\cos(k)\cos(k') - 1)}$$

with the corresponding energy eigenstates:

$$\langle x|\psi_k^{\mathrm{R}}\rangle = \psi_k^{\mathrm{R}}(x) = \begin{cases} a^{\mathrm{R}}\,T^{\mathrm{R}}(k)\,\mathrm{e}^{-\mathrm{i}kx} & x \le -1 \\ a_3(k)\,\mathrm{e}^{\mathrm{i}k'x} + a_4(k)\,\mathrm{e}^{-\mathrm{i}k'x} & 0 \le x \le d-1 \\ a^{\mathrm{R}}\left(\mathrm{e}^{-\mathrm{i}kx} + R^{\mathrm{R}}(k)\,\mathrm{e}^{\mathrm{i}kx}\right) & x \ge d \end{cases} \tag{2.11}$$

We notice that $T^{\mathrm{L}}(k) = T^{\mathrm{R}}(k)$. Hence, we can just use $T(k) := T^{\mathrm{L}}(k) = T^{\mathrm{R}}(k)$ as the transmission coefficient. Correspondingly, we see that $R^{\mathrm{L}}(k) = \mathrm{e}^{\mathrm{i}(2d-2)k} R^{\mathrm{R}}(k)$, which, in particular, implies $|R^{\mathrm{L}}(k)|^2 = |R^{\mathrm{R}}(k)|^2$. These results are expected due to the translational invariance of the underlying Hamiltonian (2.2). Additionally, a longer calculation yields

$$T(-k) = [T(k)]^*, \quad R^{\mathrm{L}}(-k) = [R^{\mathrm{L}}(k)]^*, \quad R^{\mathrm{R}}(-k) = [R^{\mathrm{R}}(k)]^*, \tag{2.12a}$$

$$T(k)[R^{\mathrm{L}}(k)]^* + R^{\mathrm{R}}(k)[T(k)]^* = 0, \tag{2.12b}$$

$$|T(k)|^2 + |R^{\mathrm{L}}(k)|^2 = |T(k)|^2 + |R^{\mathrm{R}}(k)|^2 = 1. \tag{2.12c}$$

These are the unitarity conditions of the corresponding S-matrix [9, p. 107] and guarantee the conservation of probability current throughout the potential barrier. We will come back to these equations in Sec. 2.4.

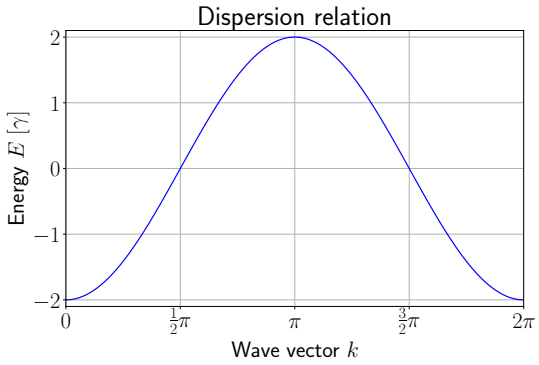

Figure 2.1: Dispersion relation $E(k)$ according to Eq. (2.4).

From the dispersion relation (2.4), which is plotted in Fig. 2.1, we see that, for each energy value $-2\gamma < E < 2\gamma$ inside the band, we find two k for a wave coming in from the left side and two k for a wave coming in from the right side; which gives a total of four states per energy value. Since $k \in [0, 2\pi)$, there is only one k for the energy values $E \in \{-2\gamma, 2\gamma\}$ at the edge of the band; regarding both directions of propagation, we get a total of two states each. In Sec. 2.4, we will find which of these energy states are actually linearly independent.

Finally, using Eq. (2.4), we plot the absolute square values of the transmission and reflection coefficient for a barrier thickness of $d = 10$ in dependency of the eigenstate energy E in Fig. 2.2. As expected, in chart (a) where $\varepsilon = 0$ (i.e. the barrier does not exist at all), there is no reflection. Furthermore, we again notice that the absolute squares of the coefficients always sum up to 1. And third, we find that there is almost no transmission at energies $E < \varepsilon - 2\gamma$. So as mentioned in the introduction, we see that the potential barrier indeed acts as a high-pass filter. Only in the logarithmic plots in the insets of (c) and (d), we see that the transmission coefficient remains finite at these energies and increases significantly for higher energies. According to the dispersion relation (2.4), $k' \notin \mathbb{R}$ for these energy values, i.e. these are the quantum tunneling eigenstates (type 2). Naturally, it is expected that transmission mediated by quantum tunneling is much less intense than through ordinary propagation. Conclusively, we can state that $|T|^2$ and $|R^{\mathrm{L}}|^2 = |R^{\mathrm{R}}|^2$ behave as usual.

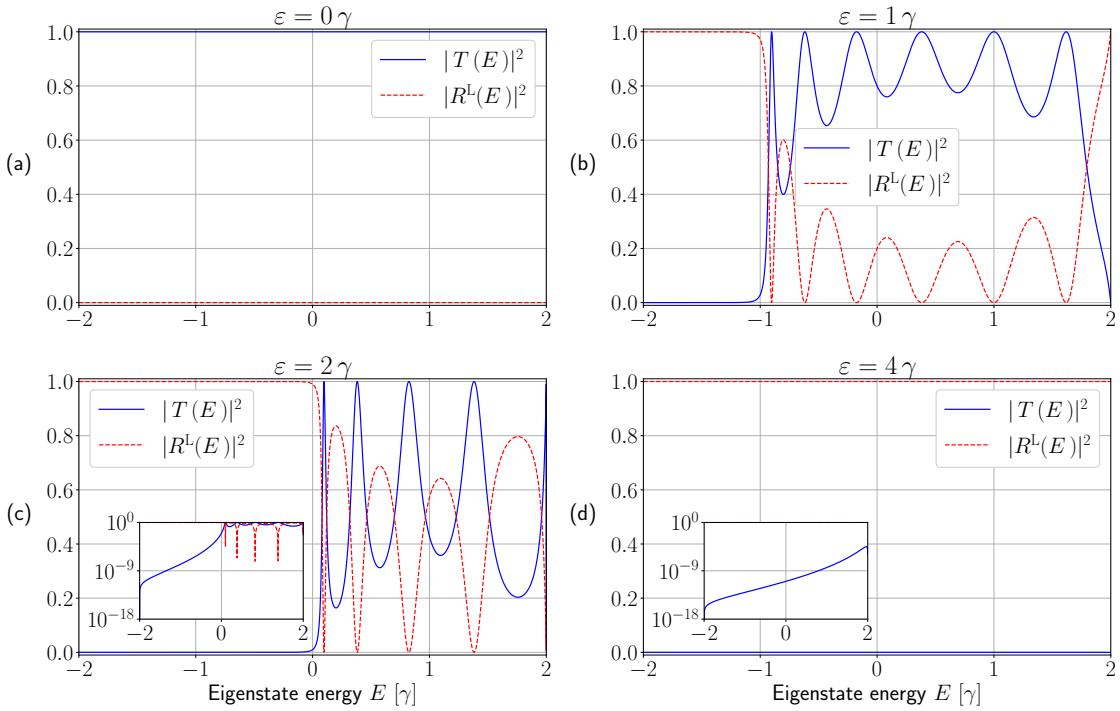

Figure 2.2: Absolute square values of the transmission and reflection coefficient in dependency of the eigenstate energy E for a barrier thickness of $d = 10$ and four different barrier heights ε. It can be seen that there is almost no transmission at energies $E < \varepsilon - 2\gamma$, which is the quantum tunneling region; though we see from the semi-logarithmic inset plots that the transmission coefficient is not quite zero and even increases significantly with increasing energy. Hence, we note that, as expected, the potential barrier acts as a high-pass filter.

2.3 Eigenstates type 3 - resonance states

In this section, we examine the energy eigenstates defined by Eq. (2.3) where $k \notin \mathbb{R}$, which we will call the resonance states. Since the energy $E(k)$ (according to Eq. (2.4)) must be real, this requires $\mathrm{Re}(k) = n\pi, n \in \mathbb{Z}$. As the stationary wave ansatz is 2π-periodic, we limit our review to $\mathrm{Re}(k) \in \{0, \pi\}$ with no loss of generality. Furthermore, we restrict our analysis to $\mathrm{Im}(k) > 0$; the reason for this is explained later.

If $\mathrm{Im}(k) > 0$, $\mathrm{e}^{\mathrm{i}kx} \to \infty$ as $x \to -\infty$ and $\mathrm{e}^{-\mathrm{i}kx} \to \infty$ as $x \to +\infty$. Hence, for the eigenstate to be normalizable, the coefficients $a_1(k)$ and $a_6(k)$ must vanish. To find the position space representation $\psi_k(x)$ of these new resonance states, we can use our result $|\psi_k^{\mathrm{L}}\rangle$ from the previous section (Eq. (2.8)) because $a_1(k) = 0, a_6(k) = 0$ is just a special case of $a_6(k) = 0$, which was considered there. Since $a_1(k) = 0$ now, we get that the transmission coefficient $T^{\mathrm{L}}(k) := \frac{a_5(k)}{a_1(k)}$ and the reflection coefficient $R^{\mathrm{L}}(k) := \frac{a_2(k)}{a_1(k)}$ diverge, or equivalently

$$\frac{1}{|T^{\mathrm{L}}(k)|^2} = 0, \quad \frac{1}{|R^{\mathrm{L}}(k)|^2} = 0. \tag{2.13}$$

It is clear that these conditions will only be satisfied for specific k. For a general barrier width d, these equations are transcendental. Given a specific d, we can use the trigonometric addition theorems and Eq. (2.4) to express $|T^{\mathrm{L}}(k)|^2$ and $|R^{\mathrm{L}}(k)|^2$ (as

given by Eqs. (2.6) and (2.7)) in terms of the sine and cosine of k'. This way, we get two trigonometric polynomials, for which we (numerically) find $2d-2$ roots. Since $E(k')$ must be real, only roots with $\cos(k') \in \mathbb{R}$ and, as required above, $\mathrm{Im}(k) > 0$ will give actual eigenstates. It turns out that, depending on ε, we find at most d such roots.

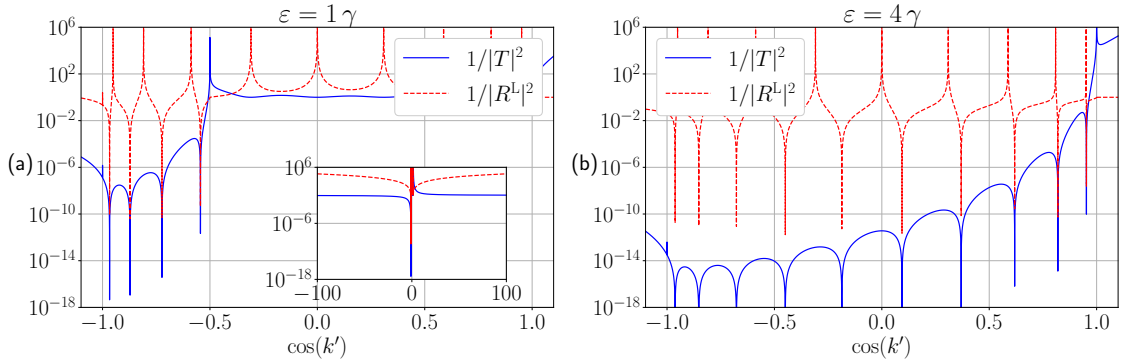

Figure 2.3: Inverse absolute square values of the transmission and reflection coefficient T and R^{L}, respectively, in dependency of the cosine of the wave vector k' inside the barrier region for $d = 10$ and two different barrier heights ε. From the inset in (a), we can see that the coefficients behave regularly for the most values $\cos(k') \in \mathbb{R}$. Their poles, which define the resonance states according to Eq. (2.13), lie always in the interval $-1 \leq \cos(k') \leq \min(1, \varepsilon/2\gamma - 1)$. We also notice that the two coefficients have exactly the same poles, which directly follows from their definition in Eqs. (2.6) and (2.7).

In Fig. 2.3, $1/|T^{\mathrm{L}}(k)|^2$ and $1/|R^{\mathrm{L}}(k)|^2$ are shown in dependency of $\cos(k')$ for a barrier width of $d = 10$ and two different barrier heights ε. From the inset in (a), we see that both coefficients behave regularly for most values $\cos(k') \in \mathbb{R}$. By probing many different $\varepsilon > 0$, it eventually turns out that the roots always lie in the interval $-1 \leq \cos(k') \leq \min(1, \varepsilon/2\gamma - 1)$ and thus belong to $k' \in \mathbb{R}$. This also defines their energies to be in the interval $\max(\varepsilon - 2\gamma, 2\gamma) \leq E(k') \leq \varepsilon + 2\gamma$, which is easy to understand: The resonance states lie in the same energy band $-2\gamma \leq E \leq 2\gamma$ as the band states but are shifted to higher energies by precisely the barrier height ε; the overall lower bound $E > 2\gamma$ originates from the requirement $k \notin \mathbb{R}$. As can be seen in plot (b), the maximum number of d roots is reached given a sufficiently large ε.

Now, we label the solutions k' of Eq. (2.13) with an index $l \in \{1, ..., B\}$ where $B \leq d$ denotes the number of solutions in dependency of the barrier height ε. Using Eq. (2.4), we get the corresponding wave vectors k outside of the barrier. Here, we must be careful to choose the correct branch of the inverse cosine function such that the above requirements ($\mathrm{Re}(k) \in \{0, \pi\}$ and $\mathrm{Im}(k) > 0$) are met. With this in mind, we get

$$k_l = 2\pi - \arccos\left(\cos(k'_l) - \frac{\varepsilon}{2\gamma}\right) =: \pi + \mathrm{i}\kappa_l, \tag{2.14}$$

where $\arccos(...)$ denotes the principal branch of the arcus cosine. The real part of k_l happens to be π for all k'_l and we label the imaginary part with κ_l as indicated above. Analogously, we label the associated energy eigenvalues with $E_l := E(\pi + \mathrm{i}\kappa_l)$.

For sufficiently small d, we can carry out these calculations analytically. As an example, we present the resonance states for $d = 2$:

$$\begin{aligned} \kappa_1 &= \ln\left(\frac{\varepsilon}{\gamma} + 1\right), & E_1 &= 2\gamma + \frac{\varepsilon^2}{\varepsilon + \gamma}, \\ \kappa_2 &= \ln\left(\frac{\varepsilon}{\gamma} - 1\right), & E_2 &= -2\gamma + \frac{\varepsilon^2}{\varepsilon - \gamma}. \end{aligned} \tag{2.15}$$

The first resonance state κ_1 thereby exists for every barrier height $\varepsilon > 0$; the second state κ_2 exists only if $\varepsilon > 2\,\gamma$.

Finally, we can write down the position space representation of the found eigenstates, which we label with $|\psi_{\kappa_l}\rangle$ (similar to Eq. (2.8)):

$$\langle x|\psi_{\kappa_l}\rangle = \psi_{\kappa_l}(x) = \begin{cases} a_{2,l}\,(-1)^x\,\mathrm{e}^{\kappa_l x} & x \leq -1 \\ a_{3,l}\,\mathrm{e}^{\mathrm{i}k_l' x} + a_{4,l}\,\mathrm{e}^{-\mathrm{i}k_l' x} & 0 \leq x \leq d-1 \\ a_{5,l}\,(-1)^x\,\mathrm{e}^{-\kappa_l x} & x \geq d \end{cases} \tag{2.16}$$

Technically, the coefficients $a_{2,l}, ..., a_{5,l}$ could be calculated by solving again the continuity conditions (2.5). However, we will find an easier way to compute them in the next section; hence, we leave them undefined for now.

2.4 Ortho-normalization of eigenstates

After having determined the band states and resonance states in the previous sections, we now have to orthogonalize and normalize these. The resonance states' energies are not degenerate and do not overlap with the band states; therefore, they are inevitably orthogonal. Furthermore, they are the discrete part of the energy spectrum; hence, they can be normalized by requiring that

$$\sum_{x=-\infty}^{\infty} \left|\langle x|\psi_{\kappa_l}\rangle\right|^2 = 1. \tag{2.17}$$

However, later in this section, we will find a more advantageous way of normalizing the resonance states; thus, we will not solve this equation now.

Since the band states defined by Eqs. (2.8) and (2.11) represent the continuous part of our spectrum, they cannot be normalized individually. Instead, we use the fact that the total spectrum of the Hamiltonian is complete together with the fact that the position eigenstates are by definition orthogonal to find the normalization constants $a^{\mathrm{L}}, a^{\mathrm{R}}$. Before doing so, however, we have to take care of the degeneracy of the band states. As mentioned before, for every energy $-2\gamma < E < 2\gamma$, there exist two corresponding wave vectors $k_1 = \arccos(-E/2\gamma), k_2 = 2\pi - \arccos(-E/2\gamma)$ for each propagation direction $|\psi_k^{\mathrm{L}}\rangle\,, |\psi_k^{\mathrm{R}}\rangle$; hence, we have four band states per energy value. To figure out which of them are actually linearly independent, we calculate the so-called Casoratian according to [28, pp. 67, 71]:

$$C(x) = \det \begin{pmatrix} \psi_1(x) & \psi_2(x) & \dots & \psi_n(x) \\ \psi_1(x+1) & \psi_2(x+1) & \dots & \psi_n(x+1) \\ \vdots & \vdots & \ddots & \vdots \\ \psi_1(x+n-1) & \psi_2(x+n-1) & \dots & \psi_n(x+n-1) \end{pmatrix}.$$

This is basically the analogue of the Wronskian for difference equations; and correspondingly, a non-vanishing Casoratian implies that $\{\psi_1, ..., \psi_n\}$ are linearly independent. We find that all four band states are pairwise linearly independent but any three of them are linearly dependent. This implies that the degeneracy is two and we can arbitrarily choose any pair of them as our basis. However, no matter which pair of band states we choose, if we attempt to find the appropriate normalization as described above, we end up with an integral that cannot be solved in general. To resolve this issue, we include all four band states in the partition of unity

$$\sum_{l=1}^{B} |\psi_{\kappa_l}\rangle \langle\psi_{\kappa_l}| + \int_0^{2\pi} \mathrm{d}k\, |\psi_k^{\mathrm{L}}\rangle \langle\psi_k^{\mathrm{L}}| + \int_0^{2\pi} \mathrm{d}k\, |\psi_k^{\mathrm{R}}\rangle \langle\psi_k^{\mathrm{R}}| = \mathbb{1}, \tag{2.18}$$

with the additional condition $a^{\mathrm{L}} = a^{\mathrm{R}} =: a$. Admittedly, this means that we integrate twice over all band states; but this is not an issue if we choose the normalization constant properly.

Multiplying this ansatz with $\langle y|$ from the left and $|x\rangle$ from the right, using the unitarity conditions (2.12) and also the integral transformation $k \to 2\pi - k$, we get

$$\begin{aligned} x, y \leq -1: \quad \delta_{yx} &= \sum_{l=1}^{B} |a_{2,l}|^2 \, (-1)^{x+y} \, \mathrm{e}^{\kappa_l (x+y)} \\ &\quad + 4\pi |a|^2 \delta_{yx} + 2|a|^2 \int_0^{2\pi} \mathrm{d}k \, R^{\mathrm{L}}(k) \, \mathrm{e}^{-\mathrm{i}k(x+y)}, \end{aligned} \tag{2.19a}$$

$$\begin{aligned} x, y \geq d: \quad \delta_{yx} &= \sum_{l=1}^{B} |a_{5,l}|^2 \, (-1)^{x+y} \, \mathrm{e}^{-\kappa_l (x+y)} \\ &\quad + 4\pi |a|^2 \delta_{yx} + 2|a|^2 \int_0^{2\pi} \mathrm{d}k \, R^{\mathrm{R}}(k) \, \mathrm{e}^{\mathrm{i}k(x+y)}, \end{aligned} \tag{2.19b}$$

$$\begin{aligned} x \leq -1, y \geq d: \quad 0 &= \sum_{l=1}^{B} a_{5,l} [a_{2,l}]^* \, (-1)^{x+y} \, \mathrm{e}^{\kappa_l (x-y)} \\ &\quad + 2|a|^2 \int_0^{2\pi} \mathrm{d}k \, T(k) \, \mathrm{e}^{\mathrm{i}k(y-x)}, \end{aligned} \tag{2.19c}$$

$$\begin{aligned} x \geq d, y \leq -1: \quad 0 &= \sum_{l=1}^{B} a_{2,l} [a_{5,l}]^* \, (-1)^{x+y} \, \mathrm{e}^{\kappa_l (y-x)} \\ &\quad + 2|a|^2 \int_0^{2\pi} \mathrm{d}k \, T(k) \, \mathrm{e}^{\mathrm{i}k(x-y)}. \end{aligned} \tag{2.19d}$$

To satisfy these equations, $|a|^2$ must be equal to $1/4\pi$; for convenience, we choose to set $a := 1/\sqrt{4\pi}$. Now, we subtract δ_{yx} from Eq. (2.19a). Since the integral over the reflection coefficient in that equation is 2π-periodic, we can apply an integral transformation $z := \mathrm{e}^{\mathrm{i}k}, \mathrm{d}k = \mathrm{d}z/\mathrm{i}z$, which maps the original integral over the real interval $k \in [0, 2\pi)$ to the unit circle $|z| = 1$. Using the new notation $\widetilde{R}^{\mathrm{L}}(z)$ for the reflection coefficient, such that $\widetilde{R}^{\mathrm{L}}(\mathrm{e}^{\mathrm{i}k}) := R^{\mathrm{L}}(k)$, we get:

$$\begin{aligned} x, y \leq -1: \quad \sum_{l=1}^{B} |a_{2,l}|^2 \, (-1)^{x+y} \, \mathrm{e}^{\kappa_l (x+y)} &= -\frac{1}{2\pi} \int_0^{2\pi} \mathrm{d}k \, R^{\mathrm{L}}(k) \, \mathrm{e}^{-\mathrm{i}k(x+y)} \\ &= -\frac{1}{2\pi\mathrm{i}} \oint_{|z|=1} \mathrm{d}z \, \widetilde{R}^{\mathrm{L}}(z) \, z^{-(x+y)-1} \end{aligned}$$

Using the residue theorem, we find that the integral is given by the poles of the reflection coefficient $\widetilde{R}^{\mathrm{L}}(z)$ which lie inside the unit circle. As $z = \mathrm{e}^{\mathrm{i}k}$, these poles correspond to

the poles of $R^{\mathrm{L}}(k)$ with $\mathrm{Im}(k) > 0$, i.e. the resonance states. According to Eq. (2.14), these lie at the positions $z = \mathrm{e}^{\mathrm{i}k_l} = -\mathrm{e}^{-\kappa_l}$. As a result, we find:

$$\frac{1}{2\pi\mathrm{i}} \oint_{|z|=1} \mathrm{d}z\, \widetilde{R}^{\mathrm{L}}(z)\, z^{-(x+y)-1} = \sum_{l=1}^{B} \mathrm{Res}_{-\mathrm{e}^{-\kappa_l}} \Big(\widetilde{R}^{\mathrm{L}}(z) \Big)\, (-1)^{x+y+1}\, \mathrm{e}^{\kappa_l (x+y+1)}$$

Finally, we insert the definition of the residue and back transform the integral; we get:

$$\sum_{l=1}^{B} \mathrm{Res}_{-\mathrm{e}^{-\kappa_l}} \Big(\widetilde{R}^{\mathrm{L}}(z) \Big)\, (-1)^{x+y+1}\, \mathrm{e}^{\kappa_l (x+y+1)} = \mathrm{i} \sum_{l=1}^{B} \mathrm{Res}_{\pi+\mathrm{i}\kappa_l} \Big(R^{\mathrm{L}}(k) \Big)\, (-1)^{x+y}\, \mathrm{e}^{\kappa_l (x+y)}$$

The same steps can be applied to Eqs. (2.19b) to (2.19d) as well; hence, we get a total of four new conditions:

$$\begin{aligned} x, y \leq -1: \quad & \sum_{l=1}^{B} |a_{2,l}|^2\, (-1)^{x+y}\, \mathrm{e}^{\kappa_l (x+y)} \\ & = -\mathrm{i} \sum_{l=1}^{B} \mathrm{Res}_{\pi+\mathrm{i}\kappa_l} \Big(R^{\mathrm{L}}(k) \Big)\, (-1)^{x+y}\, \mathrm{e}^{\kappa_l (x+y)} \end{aligned} \tag{2.20a}$$

$$\begin{aligned} x, y \geq d: \quad & \sum_{l=1}^{B} |a_{5,l}|^2\, (-1)^{x+y}\, \mathrm{e}^{-\kappa_l (x+y)} \\ & = -\mathrm{i} \sum_{l=1}^{B} \mathrm{Res}_{\pi+\mathrm{i}\kappa_l} \Big(R^{\mathrm{R}}(k) \Big)\, (-1)^{x+y}\, \mathrm{e}^{-\kappa_l (x+y)} \end{aligned} \tag{2.20b}$$

$$\begin{aligned} x \leq -1, y \geq d: \quad & \sum_{l=1}^{B} a_{5,l} [a_{2,l}]^*\, (-1)^{x+y}\, \mathrm{e}^{\kappa_l (x-y)} \\ & = -\mathrm{i} \sum_{l=1}^{B} \mathrm{Res}_{\pi+\mathrm{i}\kappa_l} (T(k))\, (-1)^{x+y}\, \mathrm{e}^{\kappa_l (x-y)} \end{aligned} \tag{2.20c}$$

$$\begin{aligned} x \geq d, y \leq -1: \quad & \sum_{l=1}^{B} a_{2,l} [a_{5,l}]^* (-1)^{x+y}\, \mathrm{e}^{\kappa_l (y-x)} \\ & = -\mathrm{i} \sum_{l=1}^{B} \mathrm{Res}_{\pi+\mathrm{i}\kappa_l} (T(k))\, (-1)^{x+y}\, \mathrm{e}^{\kappa_l (y-x)} \end{aligned} \tag{2.20d}$$

These equations must be satisfied for every pair x, y as given on the left side; moreover, the exponential functions $\mathrm{e}^{\kappa_l \cdots}$ are linearly independent because the values κ_l are by definition pairwise distinct. This implies that Eqs. (2.20a) to (2.20d) are not only satisfied in total but also for each individual summand $l \in \{1, ..., B\}$, i.e.

$$|a_{2,l}|^2 = -\mathrm{i}\, \mathrm{Res}_{\pi+\mathrm{i}\kappa_l} \Big(R^{\mathrm{L}}(k) \Big), \tag{2.21a}$$

$$|a_{5,l}|^2 = -\mathrm{i}\, \mathrm{Res}_{\pi+\mathrm{i}\kappa_l} \Big(R^{\mathrm{R}}(k) \Big), \tag{2.21b}$$

$$a_{5,l}\, [a_{2,l}]^* = -\mathrm{i}\, \mathrm{Res}_{\pi+\mathrm{i}\kappa_l} \Big(T(k) \Big) = a_{2,l}\, [a_{5,l}]^*. \tag{2.21c}$$

These relations allow us to easily compute the absolute values of the resonance states' coefficients $a_{2,l}, a_{5,l}$ without solving the continuity conditions (2.5) and the normalization condition (2.17), respectively. Since the complex phases of these coefficients are not relevant for our further calculations, as we will see, there is indeed no need to solve said additional conditions.

As an example, we calculate the coefficients of the resonance states for $d = 2$ corresponding to κ_1, κ_2 from Eq. (2.15):

$$\begin{aligned} -\mathrm{i}\,\mathrm{Res}_{\pi+\mathrm{i}\kappa_1}(T(k)) &= \frac{\varepsilon\,(\varepsilon+2\gamma)}{2\gamma\,(\gamma+\varepsilon)}, \qquad -\mathrm{i}\,\mathrm{Res}_{\pi+\mathrm{i}\kappa_1}\Big(R^{\mathrm{R}}(k)\Big) = \frac{\varepsilon\,(\varepsilon+2\gamma)}{2\gamma^2}, \\ -\mathrm{i}\,\mathrm{Res}_{\pi+\mathrm{i}\kappa_2}(T(k)) &= \frac{\varepsilon\,(\varepsilon-2\gamma)}{2\gamma\,(\gamma-\varepsilon)}, \qquad -\mathrm{i}\,\mathrm{Res}_{\pi+\mathrm{i}\kappa_2}\Big(R^{\mathrm{R}}(k)\Big) = \frac{\varepsilon\,(\varepsilon-2\gamma)}{2\gamma^2}. \end{aligned} \tag{2.22}$$

Technically, we could repeat the same calculation also with $0 \leq x, y \leq d-1$ and even find similar equations for the coefficients $a_{3,l}, a_{4,l}$; but they are also not utilized in the later chapters.

This entire calculation now justifies our choice to consider only resonance states with $\mathrm{Im}(k) > 0$. If instead, we had also included resonance states with $\mathrm{Im}(k) < 0$, these would give additional summands on the left side of Eqs. (2.20a) to (2.20d) (with $a_{1,l}, a_{6,l}$ instead of $a_{2,l}, a_{5,l}$). However, the contour integrals over $\widetilde{R}^{\mathrm{L}}(z), \widetilde{R}^{\mathrm{R}}(z), \widetilde{T}(z)$ would not be altered; hence, there would not be any corresponding additional summands on the right side. Similar to Eqs. (2.21a) to (2.21c), we would get

$$\mathrm{Im}(k) < 0: \quad |a_{1,l}|^2 = |a_{6,l}|^2 = a_{6,l}\,[a_{1,l}]^* = a_{1,l}\,[a_{6,l}]^* = 0.$$

Since the other coefficients $a_{2,l}, a_{5,l}$ also have to vanish for $\mathrm{Im}(k) < 0$ (because $\mathrm{e}^{\mathrm{i}kx} \to \infty$ as $x \to +\infty$ and $\mathrm{e}^{-\mathrm{i}kx} \to \infty$ as $x \to -\infty$), these states would vanish everywhere; i.e. such additional solutions to Eq. (2.13) would not produce any further eigenstates.

2.5 Verification through numerical simulation

In this paragraph, the analytic results from the previous sections are verified through numerical simulation. For this purpose, we consider a finite line of discrete lattice sites at positions $x \in \{-N/2, -N/2+1, ..., N/2-1\}, N \in 2\mathbb{N}$. Analogous to Eq. (2.2), we can define the Hamiltonian $\mathcal{H}_N$ for this finite system by

$$\mathcal{H}_N = -\gamma \sum_{x=-N/2}^{N/2-2} \left(|x\rangle\langle x+1| + |x+1\rangle\langle x|\right) + \varepsilon \sum_{x=0}^{d-1} |x\rangle\langle x|\,. \tag{2.23}$$

In the first step of verification, we diagonalize this Hamiltonian using the function `numpy.linalg.eig()` from the Python library NumPy [29]. In Fig. 2.4, the resulting eigenvalues are plotted for different barrier heights $\varepsilon \in \{0.0\,\gamma, 0.1\,\gamma, ..., 5.0\,\gamma\}$ with $N = 2000, d = 10$. We see that most eigenvalues indeed lie in the energy band $-2\gamma \leq E \leq 2\gamma$, just like we found analytically for the infinite line. Furthermore, depending on the barrier height ε, there exist up to $d = 10$ eigenvalues $E > 2\gamma$. To decide whether these eigenvalues correspond to the resonance states which we found analytically, we infer the values $\cos(k')$ (according to Eq. (2.4)) from the eigenvalues, and draw them as dash-dotted vertical lines into Fig. 2.5, similar to Fig. 2.3. In fact, the figure shows that the eigenvalues from the diagonalization coincide with the roots of Eq. (2.13).

Finally, we also insert the band states $|\psi_k^{\mathrm{L}}\rangle$ from Eq. (2.8) into the eigenvalue equation $(\mathcal{H}_N - E(k)\mathbb{1})\,|\psi_k\rangle = 0$ of the finite line, i.e. we define the corresponding finite-size band states by

$$\langle x|\psi_k^N\rangle = \psi_k^N(x) = a_k^N \cdot \begin{cases} \psi_k^{\mathrm{L}}(x) & -N/2 \leq x \leq N/2-1 \\ 0 & \text{otherwise,} \end{cases}$$

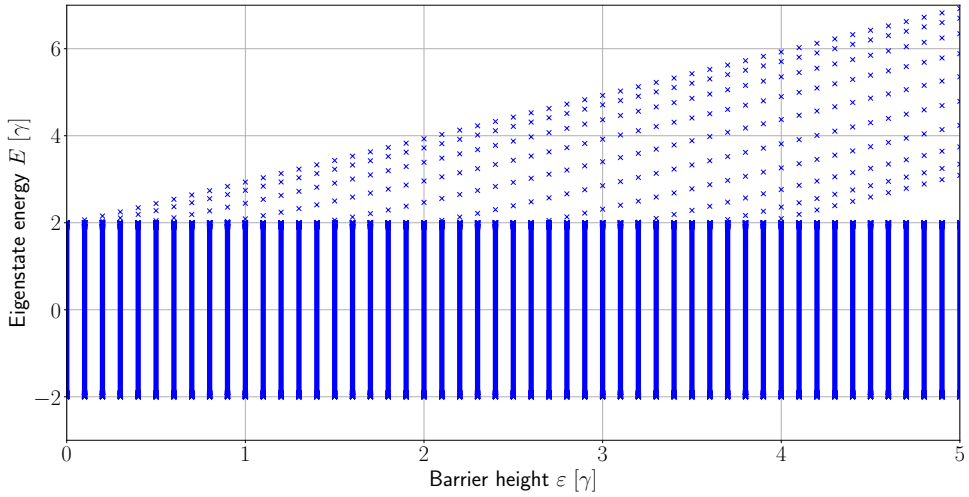

Figure 2.4: Numerically calculated energy eigenvalues of the Hamiltonian (2.23) for $d = 10, N = 2000$ and different barrier heights $\varepsilon \in \{0.0\,\gamma, 0.1\,\gamma, ..., 5.0\,\gamma\}$. Each cross stands for one eigenvalue. Obviously, the 'energy band' $-2\gamma \leq E \leq 2\gamma$ is not truly continuous in the considered finite case; nonetheless, the eigenvalues lie so dense in this interval that it appears as a band.

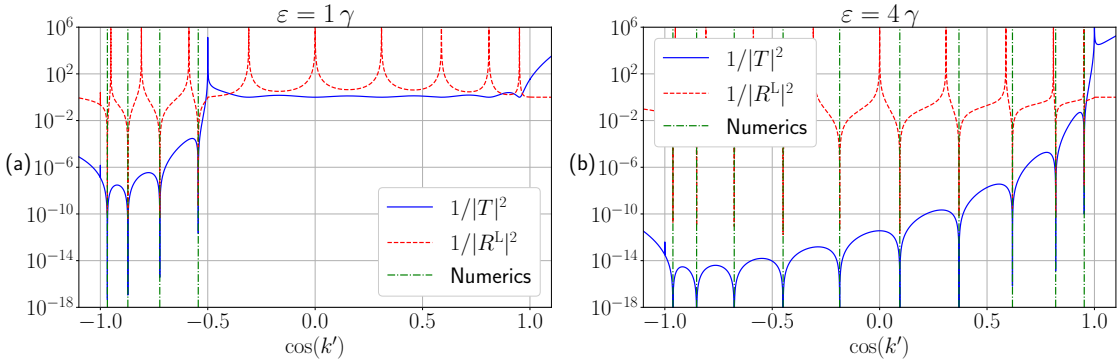

Figure 2.5: Inverse absolute square values of the transmission and reflection coefficient in dependency of the cosine of the wave vector k' inside the barrier region for $d = 10$ and two different barrier heights ε (similar to Fig. 2.3). The dash-dotted vertical lines correspond to the energy eigenvalues $E > 2\gamma$ from the numerical diagonalization for $N = 2000$ (see Fig. 2.4). It can be seen that the numerically computed eigenvalues coincide with the poles of the two coefficients as expected from our analytic consideration.

where the constant a_k^N is chosen such that $\sum_{x=-N/2}^{N/2-1} |\langle x|\psi_k^N\rangle|^2 = 1$. Furthermore, we have to find the appropriate wave vectors k which actually give an eigenstate in the finite case. By considering two phantom lattice sites at $x = -N/2 - 1$ and $x = N/2$ with Dirichlet boundary conditions [26, p. 15.10], we find that these wave vectors are given by $k_s = s\pi/(N+1), s \in \{1, ..., N\}$. Now, for all valid k_s and barrier heights

$\varepsilon \in \{0.0\,\gamma, 0.1\,\gamma, ..., 5.0\,\gamma\}$, we calculate the square norm of the eigenvalue equation

$$q := \sum_{x=-N/2}^{N/2-1} \left| \langle x | \left(\mathcal{H}_N - E(k) \mathbb{1} \right) | \psi_k^N \rangle \right|^2 ,$$

whereat $q = 0$ implies that $|\psi_k^N\rangle$ is an eigenstate of $\mathcal{H}_N$. We find that the maximum value among all said parameters is $q = 1.396 \cdot 10^{-6}$, which is already quite promising; but if we also omit the edge points to reduce boundary effects, such that the above sum only considers $-N/2+1 \leq x \leq N/2-2$, we find a maximum as low as $q' = 2.897 \cdot 10^{-24}$. This means that, apart from the boundary lattice sites, our solution for the infinite line fits the solution of the finite problem up to a relative error of the order of 10^{-24} (10^{-12} for the non-squared complex amplitudes, respectively); which again verifies our analytic results.

Chapter 3

Unitary time evolution

3.1 General aspects

In this chapter, we determine the unitary time evolution of a particle initially prepared in some position eigenstate $|x\rangle$, i.e. we calculate the complex amplitudes $\langle y|U(t)|x\rangle$ where $U(t) = \mathrm{e}^{-\mathrm{i}\mathcal{H}t/\hbar}$ denotes the unitary time evolution operator. Using the spectral decomposition (2.18), we can represent the unitary through the energy eigenvalues and eigenstates:

$$\begin{aligned}\langle y|U(t)|x\rangle = \langle y| \Bigg(&\sum_{l=1}^{B} \mathrm{e}^{-\mathrm{i}E_l t/\hbar} \left|\psi_{\kappa_l}\right\rangle \left\langle\psi_{\kappa_l}\right| \\ &+ \int_0^{2\pi} \mathrm{d}k\, \mathrm{e}^{-\mathrm{i}E(k)t/\hbar} \left(\left|\psi_k^{\mathrm{L}}\right\rangle \left\langle\psi_k^{\mathrm{L}}\right| + \left|\psi_k^{\mathrm{R}}\right\rangle \left\langle\psi_k^{\mathrm{R}}\right| \right) \Bigg) |x\rangle\end{aligned}$$

As mentioned in the introduction, we are especially interested in the case $y = x_d \geq d, x = x_i \leq -1$, for which we get the so-called transition amplitude $\langle x_d|U(t)|x_i\rangle$, that comes up in the renewal equation (1.1). Using Eqs. (2.4), (2.8), (2.11) and (2.16) for this case, the above equation simplifies to:

$$\begin{aligned}\langle x_d|U(t)|x_i\rangle = &\sum_{l=1}^{B} a_{5,l}[a_{2,l}]^* \,(-1)^{\xi}\, \mathrm{e}^{-\kappa_l \xi - \mathrm{i}E_l t/\hbar} \\ &+ \frac{1}{2\pi} \int_0^{2\pi} \mathrm{d}k\, T(k)\, \mathrm{e}^{\mathrm{i}k\xi + 2\mathrm{i}\gamma t \cos(k)/\hbar},\end{aligned}$$

where $\xi := x_d - x_i$. If we additionally insert Eq. (2.21c), we find that the transition amplitude is completely determined by the transmission coefficient:

$$\begin{aligned}\langle x_d|U(t)|x_i\rangle = &-\mathrm{i}\sum_{l=1}^{B} \mathrm{Res}_{\pi+\mathrm{i}\kappa_l}(T(k))\,(-1)^{\xi}\, \mathrm{e}^{-\kappa_l \xi - \mathrm{i}E_l t/\hbar} \\ &+ \frac{1}{2\pi} \int_0^{2\pi} \mathrm{d}k\, T(k)\, \mathrm{e}^{\mathrm{i}k\xi + 2\mathrm{i}\gamma t \cos(k)/\hbar}\end{aligned} \tag{3.1}$$

Furthermore, we seek to quantify the time evolution for $y = x = x_d \geq d$, for which we get the so-called return amplitude $\langle x_d|U(t)|x_d\rangle$ (as in Eq. (1.1)). Using Eqs. (2.4), (2.8), (2.11), (2.16) and (2.21b), we find that it is mostly determined by the reflection

coefficient. However, we get an additional term that represents the free 'propagation' from $x_d \to x_d$ without penetrating the barrier:

$$\begin{aligned}\langle x_d|U(t)|x_d\rangle = &-\mathrm{i}\sum_{l=1}^{B}\mathrm{Res}_{\pi+\mathrm{i}\kappa_l}\Big(R^{\mathrm{R}}(k)\Big)\,\mathrm{e}^{-2\kappa_l x_d-\mathrm{i}E_l t/\hbar}\\ &+\frac{1}{2\pi}\int_0^{2\pi}\mathrm{d}k\,\Big(R^{\mathrm{R}}(k)\,\mathrm{e}^{2\mathrm{i}kx_d}+1\Big)\,\mathrm{e}^{2\mathrm{i}\gamma t\cos(k)/\hbar}\end{aligned} \tag{3.2}$$

If we insert the transmission and reflection coefficient (according to Eqs. (2.9) and (2.10)) into Eqs. (3.1) and (3.2), we find that the corresponding integrals cannot be solved analytically even for the thinnest barrier $d = 1$. Therefore, in the next two sections, we evaluate both integrals by the method of steepest descents in the limit $t \to \infty$.

3.2 Asymptotic approximation of the transition amplitude for $t \to \infty$

In this section, we seek an asymptotic approximation of the transition amplitude integral in Eq. (3.1) for $t \to \infty$:

$$I_T(t) := \frac{1}{2\pi}\int_0^{2\pi}\mathrm{d}k\,\underbrace{T(k)\,\mathrm{e}^{\mathrm{i}k\xi}}_{=:\,g(k)}\,\mathrm{e}^{\overbrace{2\mathrm{i}\gamma t\cos(k)/\hbar}^{=:\,tf(k)}} \tag{3.3}$$

For this, we first define the exponent function $f(k)$ and the coefficient function $g(k)$ as above. Now, we interpret the integral as a path integral in the complex plane and apply the method of steepest descents according to [30, pp. 280-302]. The main idea is to use the Cauchy-Goursat theorem to reshape the original integration contour in such a way that we can efficiently approximate the resulting integral with a Gaussian integral. To achieve this, we start by finding the points k_n where $f(k)$ is stationary:

$$\frac{\mathrm{d}f}{\mathrm{d}k} = 0 \quad \Rightarrow \quad \sin(k) = 0 \quad \Rightarrow \quad k_n = n\pi, n \in \mathbb{Z}.$$

Since $f(k)$ is analytic, the Cauchy-Riemann equations apply and guarantee that the real part $\mathrm{Re}(f(k))$ is a harmonic function (in terms of the real and imaginary part of k). From this follows that $|\mathrm{e}^{tf(k)}| = \mathrm{e}^{t\,\mathrm{Re}(f(k))}$ has a saddle point for each k_n. Now, we use this general result to deform the original integral contour in such a way that the resulting contour crosses the saddle points k_n and follows the path for which $|\mathrm{e}^{tf(k)}|$ has its steepest descent around each k_n. Following again from the Cauchy-Riemann equations, the steepest contours are contours of constant imaginary part, i.e. we look for contours

$$C = \mathrm{Im}(f(k)) \quad \Rightarrow \quad \cosh(\mathrm{Im}(k)) = \frac{\hbar C}{2\gamma\cos(\mathrm{Re}(k))},$$

where we used $\cos(x+\mathrm{i}y) = \cos(x)\cosh(y) - \mathrm{i}\sin(x)\sinh(y)$ [27, p. 74]. The curves of interest are those which pass through the saddle points k_n:

$$C_n = \mathrm{Im}(f(k_n)) = (-1)^n\,\frac{2\gamma}{\hbar} \quad \Rightarrow \quad \cosh(\mathrm{Im}(k)) = \frac{(-1)^n}{\cos(\mathrm{Re}(k))}.$$

However, the inverse hyperbolic cosine function is ambiguous; hence, the above condition does not yield an actual contour at first. Instead, we find two separate differentiable contours which satisfy the above condition:

$$\mathrm{Im}(k) = \pm \begin{cases} \arccos\left(\frac{(-1)^n}{\cos\left(\mathrm{Re}(k)\right)}\right) & k_n - \pi/2 \leq \mathrm{Re}(k) < k_n \\ -\arccos\left(\frac{(-1)^n}{\cos\left(\mathrm{Re}(k)\right)}\right) & k_n \leq \mathrm{Re}(k) < k_n + \pi/2 \end{cases}.$$

Using again the above identity for $\cos(x + \mathrm{i}y)$, we find that for even (odd) n the contour with the positive (negative) sign follows the steepest descent around k_n, while the contour with the opposite sign follows the steepest ascent. As a result, we deform the integration contour to:

$$I_T(t) \approx \frac{1}{2\pi} \int_\alpha \mathrm{d}k\, g(k)\, \mathrm{e}^{tf(k)},$$

$$\alpha: \quad \mathrm{Im}(k) = \begin{cases} -\operatorname{arcosh}\left(\frac{1}{\cos(\mathrm{Re}(k))}\right) & 0 \leq \mathrm{Re}(k) < \pi/2 \\ -\operatorname{arcosh}\left(\frac{-1}{\cos(\mathrm{Re}(k))}\right) & \pi/2 \leq \mathrm{Re}(k) < \pi \\ \operatorname{arcosh}\left(\frac{-1}{\cos(\mathrm{Re}(k))}\right) & \pi \leq \mathrm{Re}(k) < 3\pi/2 \\ \operatorname{arcosh}\left(\frac{1}{\cos(\mathrm{Re}(k))}\right) & 3\pi/2 \leq \mathrm{Re}(k) < 2\pi \end{cases},$$

which is also shown in Fig. 3.1. It actually consists of three separate parts that are 'connected' at $k \to \pi/2 - \mathrm{i}\infty, k \to 3\pi/2 + \mathrm{i}\infty$. Furthermore, at these connecting points, the imaginary part of $f(k)$ changes from $+2\gamma/\hbar$ to $-2\gamma/\hbar$ and vice versa. In the figure, we also marked the exemplary poles of the transmission coefficient for $d = 10, \varepsilon = 2.5\,\gamma$ (determined numerically). We find that some poles (drawn in red color) indeed lie between the original and the deformed integral contour, and, hence, must be taken into account when we reshape the contour (which is also why we put an $\approx$ sign in the above equation).

According to the residue theorem, each pole of $T(k)$ between the original and reshaped integration path contributes its residue times the remaining integrand evaluated at its position to the total integral. Since the relevant poles lie at $0 < \mathrm{Re}(k) < \pi, \mathrm{Im}(k) < 0$, the resulting terms will be proportional to $\mathrm{e}^{-\lambda t}$ for some λ with $\mathrm{Re}(\lambda) > 0$ (where we again used $\cos(x + \mathrm{i}y) = \cos(x)\cosh(y) - \mathrm{i}\sin(x)\sinh(y)$ [27, p. 74]). This means, however, that they decrease faster than any polynomial of t; and we will eventually find that the remaining integral gives polynomials in t. Hence, it seems reasonable to neglect those poles after all.

Before we continue approximating the integral, we use the integrand's 2π-periodicity to shift the integration path from $0 \leq \mathrm{Re}(k) < 2\pi$ to $-\pi/2 \leq \mathrm{Re}(k) < 3\pi/2$. This way, we get an integral contour that consists of two parts that cross the two saddle points

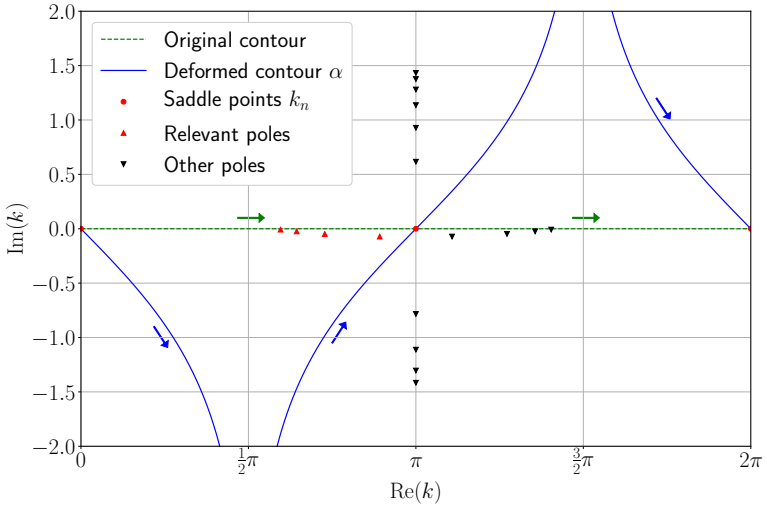

Figure 3.1: Original and deformed integration contour of the time evolution integral (3.3). At $\mathrm{Re}(k) \in \{\pi/2, 3\pi/2\}$, the deformed contour goes up to $\mathrm{Im}(k) = \pm\infty$. The triangles mark the exemplary positions of the poles of the transmission coefficient for $d = 10, \varepsilon = 2.5\,\gamma$ according to Eq. (2.6). 'Relevant' poles are those which lie in between the original and deformed integral contour and must, therefore, be taken into account, when we reshape the integral according to the Cauchy-Goursat theorem.

k_0, k_1 and have a single connecting point at $k \to \pi/2 - \mathrm{i}\infty$:

$$I_T(t) \approx \frac{1}{2\pi} \int_{\alpha'} \mathrm{d}k\, g(k)\, \mathrm{e}^{tf(k)},$$

$$\alpha' : \quad \mathrm{Im}(k) = \begin{cases} \operatorname{arcosh}\left(\dfrac{1}{\cos(\mathrm{Re}(k))}\right) & -\pi/2 \le \mathrm{Re}(k) < 0 \\ -\operatorname{arcosh}\left(\dfrac{1}{\cos(\mathrm{Re}(k))}\right) & 0 \le \mathrm{Re}(k) < \pi/2 \\ -\operatorname{arcosh}\left(\dfrac{-1}{\cos(\mathrm{Re}(k))}\right) & \pi/2 \le \mathrm{Re}(k) < \pi \\ \operatorname{arcosh}\left(\dfrac{-1}{\cos(\mathrm{Re}(k))}\right) & \pi \le \mathrm{Re}(k) < 3\pi/2 \end{cases}.$$

By means of the method of steepest descents, the exponent function $f(k)$ now has a constant imaginary part along the integration contour (except for the change at the connecting point $k \to \pi/2 - \mathrm{i}\infty$) and only its real part varies. Hence, we can factor out the imaginary part:

$$I_T(t) \approx \frac{1}{2\pi} \left(\mathrm{e}^{\mathrm{i}C_0 t} \int_{\alpha_0} \mathrm{d}k\, g(k)\, \mathrm{e}^{t\,\mathrm{Re}(f(k))} + \mathrm{e}^{\mathrm{i}C_1 t} \int_{\alpha_1} \mathrm{d}k\, g(k)\, \mathrm{e}^{t\,\mathrm{Re}(f(k))} \right),$$

where α_0, α_1 denote the two parts of α which cross k_0 and k_1, respectively. The asymptotic behavior of the two remaining integrals can now be found using Laplace's method [30, pp. 261-276]. For this, we parameterize the integration contour by

$$\alpha_n(s) = \overbrace{s + n\pi}^{\text{real part}} + \overbrace{\mathrm{i}\,(-1)^{1-n}\,\mathrm{sgn}(s)\operatorname{arcosh}\left(\frac{1}{\cos(s)}\right)}^{\text{imaginary part}}, \quad s \in \left[-\tfrac{\pi}{2}, \tfrac{\pi}{2}\right),$$

and approximate the exponent function $\mathrm{Re}(f(k))$ by a Taylor polynomial of degree two around the saddle points k_0, k_1:

$$\mathrm{Re}\Big(f(\alpha_n(s))\Big) \overset{s\to 0}{\sim} -\frac{2\gamma}{\hbar}s^2 + \mathcal{O}(s^3). \tag{3.4}$$

Further on, we also approximate the remaining integrand, which consists of $g(k)$ and the Jacobian determinant $\alpha_n'(s)$, around the saddle points up to second order:

$$\begin{aligned} g(\alpha_n(s))\,\alpha_n'(s) \overset{s\to 0}{\sim}\; & g(\alpha_n(0))\;\alpha_n'(0) + g'(\alpha_n(0))\left(\alpha_n'(0)\right)^2 s \\ & + \left(g(\alpha_n(0))\;\alpha_n'''(0) + g''(\alpha_n(0))\left(\alpha_n'(0)\right)^3\right)\frac{s^2}{2} + \mathcal{O}(s^3), \end{aligned}$$

where we used $\alpha_n''(0) = 0$ and $'$ denotes the derivative of g with respect to k and the derivative of α_n with respect to s, respectively. It follows the asymptotic approximation for the integral:

$$\begin{aligned} I_T(t) \overset{t\to\infty}{\sim} \frac{1}{2\pi}\sum_{n\in\{0,1\}} \mathrm{e}^{\mathrm{i}C_n t}\int_{-\infty}^{\infty}\mathrm{d}s\,\Bigg(& g(k_n)\,\alpha_n'(0) + g'(k_n)\left(\alpha_n'(0)\right)^2 s \\ & + \left(g(k_n)\,\alpha_n'''(0) + g''(k_n)\left(\alpha_n'(0)\right)^3\right)\frac{s^2}{2}\Bigg)\,\mathrm{e}^{-2\gamma t s^2/\hbar} \end{aligned} \tag{3.5}$$

The necessary derivates are:

$$\begin{aligned} \alpha_n'(0) &= \sqrt{2}\,\mathrm{e}^{(-1)^{1-n}\mathrm{i}\pi/4}, & \alpha_n'''(0) &= (-1)^{1-n}\,\mathrm{i}, \\ g(0) &= T(0), & g''(0) &= T''(0) + 2\mathrm{i}\xi\,T'(0) - \xi^2\,T(0), \\ g(\pi) &= (-1)^{\xi}\,T(\pi), & g''(\pi) &= (-1)^{\xi}\left(T''(\pi) + 2\mathrm{i}\xi\,T'(\pi) - \xi^2\,T(\pi)\right), \end{aligned}$$

The remaining Gaussian integrals are easy to compute, we get:

$$\begin{aligned} I_T(t) \overset{t\to\infty}{\sim}\; & \frac{1}{2\sqrt{\pi\gamma t/\hbar}}\left(T(0)\,\mathrm{e}^{2\mathrm{i}\gamma t/\hbar - \mathrm{i}\pi/4} + (-1)^{\xi}\,T(\pi)\,\mathrm{e}^{-2\mathrm{i}\gamma t/\hbar + \mathrm{i}\pi/4}\right) \\ & + \frac{1}{8\sqrt{\pi(\gamma t/\hbar)^3}}\Bigg(\left(T''(0) + 2\mathrm{i}\xi\,T'(0) + \left(\tfrac{1+\mathrm{i}}{4} - \xi^2\right)T(0)\right)\mathrm{e}^{2\mathrm{i}\gamma t/\hbar - 3\mathrm{i}\pi/4} \\ & \qquad + (-1)^{\xi}\left(T''(\pi) + 2\mathrm{i}\xi\,T'(\pi) + \left(\tfrac{1-\mathrm{i}}{4} - \xi^2\right)T(\pi)\right)\mathrm{e}^{-2\mathrm{i}\gamma t/\hbar + 3\mathrm{i}\pi/4}\Bigg). \end{aligned} \tag{3.6}$$

Now, when we take a closer look at the transmission coefficient (from Eq. (2.9)), we find that $T(0) = T(\pi) = 0$ because $T(k) \propto \sin(k)$. Hence, some terms in the above equation vanish. Finally, we insert our result into Eq. (3.1) and find that the asymptotic transition amplitude for $t \to \infty$ is given by

$$\begin{aligned} \langle x_d|U(t)|x_i\rangle \overset{t\to\infty}{\sim}\; & \sum_{l=1}^{B}\langle x_d|\psi_{\kappa_l}\rangle\,\langle\psi_{\kappa_l}|x_i\rangle\;\mathrm{e}^{-\mathrm{i}E_l t/\hbar} \\ & + \frac{1}{8\sqrt{\pi(\gamma t/\hbar)^3}}\left(\mathcal{T}_\xi(0)\,\mathrm{e}^{2\mathrm{i}\gamma t/\hbar - 3\mathrm{i}\pi/4} + (-1)^{\xi}\,\mathcal{T}_\xi(\pi)\,\mathrm{e}^{-2\mathrm{i}\gamma t/\hbar + 3\mathrm{i}\pi/4}\right), \end{aligned} \tag{3.7}$$

where $\mathcal{T}_\xi(k) := T''(k) + 2\mathrm{i}\xi\,T'(k)$. This equation is one of our main findings. According to our choice of $f(k)$ in Eq. (3.3), it is asymptotically valid for $t \gg \hbar\xi/2\gamma$. In this limit,

the transition amplitude $\langle x_d|U(t)|x_i\rangle$ is dominated by two terms. The transmission through the band states gives a term with a power-law decay $t^{-3/2}$ and superimposed oscillations with frequency $\pm 2\gamma/\hbar$. The amplitude of the power-law is defined by the derivatives (up to second order in our expansion) of the transmission coefficient at the edges of the energy band ($E = -2\gamma \leftrightarrow k = 0, E = +2\gamma \leftrightarrow k = \pi$) and by the distance ξ between the initial and detection site. The frequency of the oscillations is given by the width of the energy band. This result is in strong contrast to the free propagation without barrier, where $\langle x_d|U(t)|x_i\rangle$ shows a power-law decay $t^{-1/2}$ [24, 21]. Consequently, we acknowledge that the introduction of the barrier altered the spectral dimension of the system from $d_\mathrm{S} = 1$ to $d_\mathrm{S} = 3$.[1] The resonance states contribute a sum of terms which oscillate like $\mathrm{e}^{-\mathrm{i}\omega_l t}$ with a different frequency $\omega_l = E_l/\hbar$ each; so taken together they give a quasi-periodic function. The amplitudes of these terms are directly given by the overlap of the position eigenstates $|x_d\rangle, |x_i\rangle$ with the respective resonance state $|\psi_{\kappa_l}\rangle$, which is proportional to $\mathrm{e}^{-\kappa_l \xi}$ according to Eq. (2.16). In particular, this implies that for large ξ, the influence of the resonance states can be neglected for a very long time. Until beyond $t \gtrsim t_0^\mathrm{T}$ with

$$\left|\frac{\overbrace{\mathcal{T}_\xi(0) + \mathcal{T}_\xi(\pi)}^{=\mathcal{O}(\xi)}}{8\sqrt{\pi(\gamma t_0^\mathrm{T}/\hbar)^3}}\right| \approx \Bigg|\underbrace{\sum_{l=1}^{B} \langle x_d|\psi_{\kappa_l}\rangle \langle \psi_{\kappa_l}|x_i\rangle}_{=\mathcal{O}(\mathrm{e}^{-\hat{\kappa}\xi})}\Bigg|, \tag{3.8}$$

$$\Rightarrow \quad t_0^\mathrm{T} = \mathcal{O}(\xi^{2/3}\mathrm{e}^{2\hat{\kappa}\xi/3}), \quad \hat{\kappa} := \min \kappa_l.$$

After this point, the resonance states finally begin to dominate the transition amplitude.

3.3 Asymptotic approximation of the return amplitudes for $t \to \infty$

Analogous to the previous section, we now apply the method of steepest descents to find an asymptotic approximation for $t \to \infty$ of the return amplitude integral in Eq. (3.2):

$$I_R(t) := \frac{1}{2\pi}\int_0^{2\pi} \mathrm{d}k \underbrace{\left(R^\mathrm{R}(k)\,\mathrm{e}^{2\mathrm{i}kx_d} + 1\right)}_{=:g(k)} \overbrace{\mathrm{e}^{2\mathrm{i}\gamma t\cos(k)/\hbar}}^{=:tf(k)} \tag{3.9}$$

Since the exponent function $f(k)$ is exactly the same as in Eq. (3.3), the saddle points and steepest contours are the same as in the previous section. Furthermore, our considerations about the poles of the transmission coefficient also apply here because the reflection coefficient has by definition the same poles (see Eqs. (2.9) and (2.10)). Therefore, we find the same asymptotic approximation as in Eq. (3.5):

$$I_R(t) \overset{t\to\infty}{\sim} \frac{1}{2\pi}\sum_{n\in\{0,1\}} \mathrm{e}^{\mathrm{i}C_n t}\int_{-\infty}^{\infty}\mathrm{d}s \left(g(k_n)\,\alpha_n'(0) + g'(k_n)\left(\alpha_n'(0)\right)^2 s \right.$$
$$\left. + \left(g(k_n)\,\alpha_n'''(0) + g''(k_n)\left(\alpha_n'(0)\right)^3\right)\frac{s^2}{2}\right)\mathrm{e}^{-2\gamma t s^2/\hbar}$$

[1] The spectral dimension d_S is defined by the asymptotic behavior of the transition amplitude via $\langle x_d|U(t)|x_i\rangle \propto t^{-d_\mathrm{S}/2}$ [21].

However, the coefficient function $g(k)$ is different from that in Eq. (3.3); hence, we get other terms in the Taylor expansion of the remaining integrand ($g(k)$ and Jacobian determinant $\alpha_n'(s)$):

$$\begin{aligned} g(0) &= R^{\mathrm{R}}(0) + 1, & g''(0) &= R^{\mathrm{R}\prime\prime}(0) + 4\mathrm{i}x_d\, R^{\mathrm{R}\prime}(0) - 4x_d^2\, R^{\mathrm{R}}(0), \\ g(\pi) &= R^{\mathrm{R}}(\pi) + 1, & g''(\pi) &= R^{\mathrm{R}\prime\prime}(\pi) + 4\mathrm{i}x_d\, R^{\mathrm{R}\prime}(\pi) - 4x_d^2\, R^{\mathrm{R}}(\pi). \end{aligned}$$

Using these values, we get:

$$\begin{aligned} I_R(t) \overset{t\to\infty}{\sim} \frac{1}{2\sqrt{\pi\gamma t/\hbar}} \Big(\big(R^{\mathrm{R}}(0)+1\big)\, \mathrm{e}^{2\mathrm{i}\gamma t/\hbar - \mathrm{i}\pi/4} + \big(R^{\mathrm{R}}(\pi)+1\big)\, \mathrm{e}^{-2\mathrm{i}\gamma t/\hbar + \mathrm{i}\pi/4} \Big) \\ + \frac{1}{8\sqrt{\pi(\gamma t/\hbar)^3}} \Big(\Big(R^{\mathrm{R}\prime\prime}(\pi) + 4\mathrm{i}x_d\, R^{\mathrm{R}\prime}(\pi) + \big(\tfrac{1+\mathrm{i}}{4} - 4x_d^2\big)\, R^{\mathrm{R}}(0) + \tfrac{1+\mathrm{i}}{4} \Big)\, \mathrm{e}^{2\mathrm{i}\gamma t/\hbar - 3\mathrm{i}\pi/4} \\ + \Big(R^{\mathrm{R}\prime\prime}(\pi) + 4\mathrm{i}x_d\, R^{\mathrm{R}\prime}(\pi) + \big(\tfrac{1-\mathrm{i}}{4} - 4x_d^2\big)\, R^{\mathrm{R}}(\pi) + \tfrac{1-\mathrm{i}}{4} \Big)\, \mathrm{e}^{-2\mathrm{i}\gamma t/\hbar + 3\mathrm{i}\pi/4} \Big). \end{aligned}$$

When we look at the reflection coefficient (given by Eq. (2.10)), we find that $R^{\mathrm{R}}(0) = R^{\mathrm{R}}(\pi) = -1$. Hence, similar to Eq. (3.6), some terms vanish as well here. We finally insert the result into Eq. (3.2) and find that the asymptotic return amplitude for $t \to \infty$ is given by

$$\begin{aligned} \langle x_d|U(t)|x_d\rangle \overset{t\to\infty}{\sim} \sum_{l=1}^{B} \big|\langle \psi_{\kappa_l}|x_d\rangle\big|^2\, \mathrm{e}^{-\mathrm{i}E_l t/\hbar} \\ + \frac{1}{8\sqrt{\pi(\gamma t/\hbar)^3}} \big(\mathcal{R}_{x_d}(0)\, \mathrm{e}^{2\mathrm{i}\gamma t/\hbar - 3\mathrm{i}\pi/4} + \mathcal{R}_{x_d}(\pi)\, \mathrm{e}^{-2\mathrm{i}\gamma t/\hbar + 3\mathrm{i}\pi/4} \big), \end{aligned} \tag{3.10}$$

where $\mathcal{R}_{x_d}(k) := R^{\mathrm{R}\prime\prime}(k) + 4\mathrm{i}x_d\, R^{\mathrm{R}\prime}(k) + 4x_d^2$. This equation is another main result of this work. According to our choice of $f(k)$ in Eq. (3.9), it is asymptotically valid for $t \gg \hbar x_d/\gamma$. Moreover, it is very similar to Eq. (3.7); hence, within said time limit, the return amplitude $\langle x_d|U(t)|x_d\rangle$ behaves very much similar to the transition amplitude. The 'propagation' through the band states contributes a term with a power-law decay $t^{-3/2}$ with superimposed oscillations of frequency $\pm 2\gamma/\hbar$. The amplitude of the power-law is given by the reflection coefficient (and its first and second derivative in our expansion) at the edges of the energy band ($k = 0$ and $k = \pi$) and by the position of the detection site x_d. The resonance states contribute a sum of terms which oscillate like $\mathrm{e}^{-\mathrm{i}\omega_l t}$ with a different frequency $\omega_l = E_l/\hbar$ each; i.e. taken together a quasi-periodic function. The amplitudes of these terms are given by the overlap of the detection site $|x_d\rangle$ with the respective eigenstate $|\psi_{\kappa_l}\rangle$, which is proportional to $\mathrm{e}^{-\kappa_l x_d}$ according to Eq. (2.16). This implies that for a large value x_d, the impact of the resonance states can be neglected for a very long time. Until beyond $t \gtrsim t_0^{\mathrm{R}}$ with

$$\begin{aligned} \left| \frac{\overbrace{\mathcal{R}_{x_d}(0) + \mathcal{R}_{x_d}(\pi)}^{=\mathcal{O}(x_d^2)}}{8\sqrt{\pi(\gamma t_0^{\mathrm{R}}/\hbar)^3}} \right| \approx \underbrace{\sum_{l=1}^{B} \big|\langle \psi_{\kappa_l}|x_d\rangle\big|^2}_{=\mathcal{O}(\mathrm{e}^{-2\hat{\kappa}x_d})}, \\ \Rightarrow \quad t_0^{\mathrm{R}} = \mathcal{O}(x_d^{4/3}\mathrm{e}^{4\hat{\kappa}x_d/3}), \quad \hat{\kappa} := \min \kappa_l. \end{aligned} \tag{3.11}$$

After this point, the resonance states finally dominate the return amplitude. Interestingly, though, t_0^{R} and t_0^{T} (from Eq. (3.8)) have a different dependency on x_d (and x_i, respectively) because $\mathcal{R}_{x_d}(k) = \mathcal{O}(x_d^2)$ while $\mathcal{T}_\xi(k) = \mathcal{O}(\xi)$. Consequently, the time window in which the resonance states can be neglected is much longer for the return amplitude than for the transition amplitude for x_d and x_i of the same order of magnitude.

3.4 Verification through numerical simulation

In this section, we verify the asymptotic approximation for the transition and return amplitude from Eqs. (3.7) and (3.10), respectively. For this, we come back to the finite line Hamiltonian $\mathcal{H}_N$ from Eq. (2.23) and use the function `scipy.linalg.expm()` from the Python library SciPy [31] to compute the corresponding finite line unitary $U_N(t) = \mathrm{e}^{-\mathrm{i}\mathcal{H}_N t/\hbar}$. Using this unitary time evolution operator, we can numerically propagate the transition amplitude $\langle x_d|U_N(t)|x_i\rangle$ and the return amplitude $\langle x_d|U_N(t)|x_d\rangle$ on the finite lattice, corresponding to Eqs. (3.7) and (3.10) for the infinite case.

In order to compare them, we first have to calculate the residues of the transmission and reflection coefficient which appear in the resonance states' terms in Eqs. (3.7) and (3.10). In Eqs. (2.15) and (2.22), we already did this for $d = 2$; hence, we first consider this barrier width. Fig. 3.2, shows the transition amplitude $|\langle x_d|U(t)|x_i\rangle|^2$ for four different pairs x_d, x_i with $N = 2000, d = 2, \varepsilon = 2.5\,\gamma$. First, we notice that the asymptotic approximation (3.7) fits the numerical simulation very well; in particular, we also clearly see the transition from the power-law decay to the quasi-periodic function in plot (a). After $t \approx 1000\,\hbar/\gamma$, however, we see effects induced by the finite size of the simulated lattice, which is pretty easy to understand: The maximum group velocity at which a given wavefront travels on the lattice is $v_{\mathrm{g,\,max}} = \max(\hbar^{-1}\,\mathrm{d}E/\,\mathrm{d}k) = 2\gamma/\hbar$. Therefore, a wavefront needs at least a time of $t = N/v_{\mathrm{g,\,max}} = \hbar N/2\gamma$ to travel from one end of the lattice to the other. This implies that, for $t \gtrsim \hbar N/2\gamma$, finite-size effects will emerge in the simulation; which is what we observe in all four panels of Fig. 3.2. Consequently, we only simulate up to $t = \hbar N/2\gamma$ as of now.

Fig. 3.3, again shows $|\langle x_d|U(t)|x_i\rangle|^2$ for the same four pairs x_d, x_i, but with $\varepsilon = 1.9\,\gamma$. In contrast to Fig. 3.2 for $\varepsilon = 2.5\,\gamma$, we now find a large deviation between the numerics and the asymptotic expression (3.7), which becomes smaller for x_d, x_i that are further away from the barrier, however. We can understand what is going on here by taking a look at the logarithmic slopes in Fig. 3.3: The leading order of our asymptotic result (3.7) is proportional to t^{-3} (because we consider the absolute square here). The numerical simulation, on the other hand, starts with a different slope and only slowly converges to t^{-3}. This means that for the considered value of $\varepsilon = 1.9\,\gamma$, the time evolution has not yet converged to its asymptotic form in the regarded time window $t < 1000\,\hbar/\gamma$.

By trying out different barrier heights ε, we find that this always happens near values where the number of resonance states B changes (which happens at $\varepsilon = 2\,\gamma$ for $d = 2$). This can be seen especially well with a thicker barrier since the number of resonance states increases with the barrier width. However, for thicker barriers $d > 4$ the resonance states cannot be determined exactly (i.e. analytically); and consequently, we cannot analytically calculate the residues in Eq. (3.7). Therefore, we must choose coordinates x_d, x_i sufficiently far away from the barrier such that we can neglect the quasi-periodic term within our numerically accessible time window. In Fig. 3.4, we have

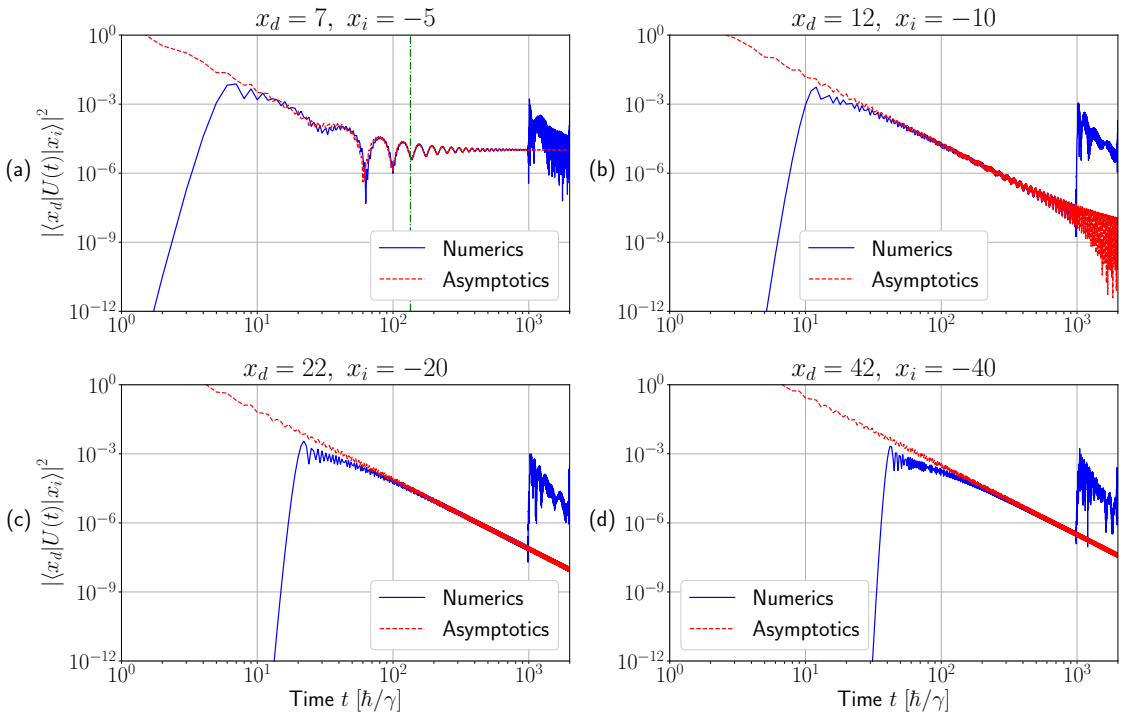

Figure 3.2: Double logarithmic plot of the transition amplitude $|\langle x_d|U(t)|x_i\rangle|^2$ for $d = 2, \varepsilon = 2.5\,\gamma$ and four different pairs x_d, x_i which lie on opposing sides of the barrier. The amplitude is calculated numerically for a finite lattice with $N = 2000$ and compared to the asymptotic expansion (3.7). It can be seen that the latter fits the former very well. In particular, we also find the transition from the power-law decay to the quasi-periodic function in plot (a), where we also marked $t_0^{\mathrm{T}} \sim \xi^{2/3}\,\mathrm{e}^{2\hat{\kappa}\xi/2}\,\hbar/\gamma$, according to Eq. (3.8), with a vertical line. Beyond $t \gtrsim 1000\,\hbar/\gamma$, finite-size effects appear and destroy the agreement.

done exactly this. It can be seen there that for $d = 10$, the transition amplitude for $\varepsilon \in \{1.9\,\gamma, 2.5\,\gamma\}$ converges pretty well to the asymptotic form within the considered time window; whereas for $\varepsilon \in \{0.4\,\gamma, 3.6\,\gamma\}$, we again find large deviations. Indeed around the latter values, the number of resonance states changes, as can be seen in panel (e).

The reason for this convergence behavior lies in our choice of $f(k)$ and $g(k)$ in Eq. (3.3). We determined the optimal integration path (i.e. the steepest descent path) with regard only to $\mathrm{e}^{tf(k)}$, thereby assuming that the remaining integrand $g(k)$ varies negligibly slowly around the resulting saddle points. The emergence of a new resonance state is, however, accompanied by a pole of $T(k)$ (and $R(k)$ as well) that lies at $k_{\mathrm{p}} \approx \pi$ very close to the saddle point at $k_1 = \pi$. This pole significantly shifts the position of the actual saddle point of the total integrand $g(k)\,\mathrm{e}^{tf(k)}$, thereby introducing a new intermediary time scale related to $|k_p - \pi|^{-1}$. Because of our choice of $f(k)$, this behavior is disregarded in our approximation though. In the future, one may, therefore, improve our steepest descents integration by including also $\ln(k - k_p)$ in the exponent function.

Eventually, we find the same behavior also for the return amplitudes $|\langle x_d|U(t)|x_d\rangle|^2$, $x_d \geq d$, with the asymptotic expression (3.10). However, as can be seen in Fig. 3.5, the convergence of the numerical simulation to the asymptotics becomes much slower

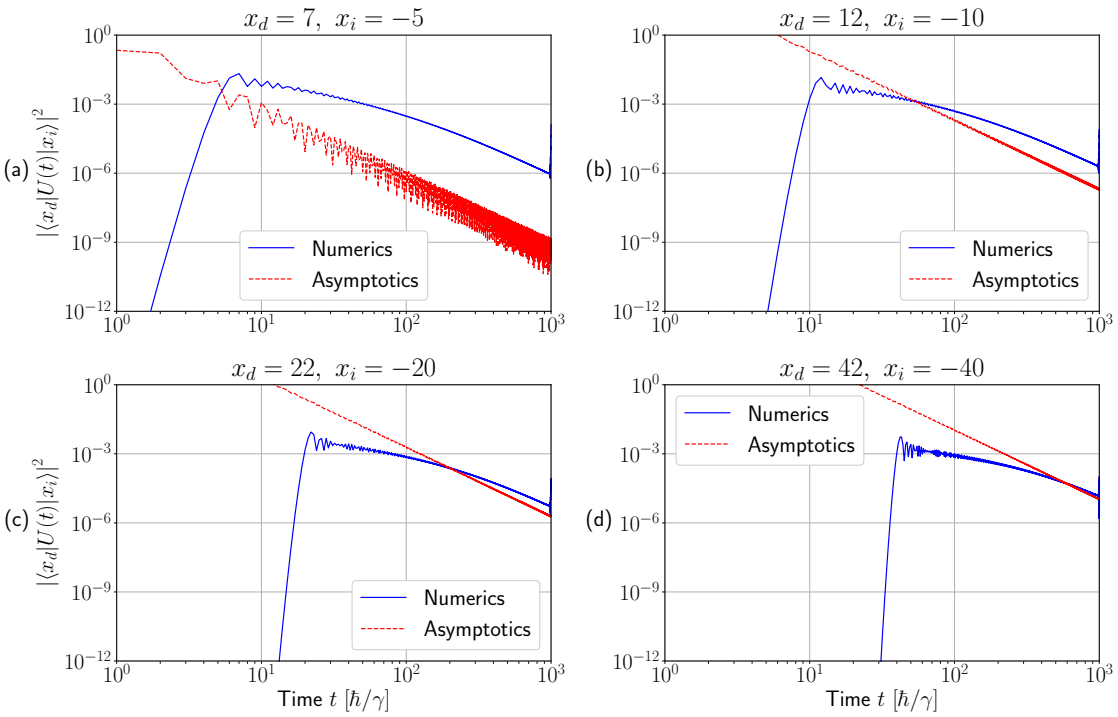

Figure 3.3: Double logarithmic plot of the transition amplitude $|\langle x_d|U(t)|x_i\rangle|^2$ for $d = 2, \varepsilon = 1.9\,\gamma$ and the same four pairs x_d, x_i as in Fig. 3.2. The amplitude is calculated numerically for a finite lattice with $N = 2000$ and compared to the asymptotic result (3.7). In contrast to Fig. 3.2, none of the four numerical simulations converges to the asymptotic approximation within the considered time window. The reason for this is the different value of the barrier height ε.

with increasing x_d. This effect is also visible in Fig. 3.2 for the transition amplitudes as x_d gets larger and x_i gets smaller, but it is much more pronounced for the return amplitudes in Fig. 3.5. Nonetheless, the effect is not surprising in general, considering that our approximation is asymptotically valid for $t \gg \hbar x_d/\gamma$, as mentioned in the previous section.

Similar to the transition amplitude, we also find poor agreement between the numerical data and the asymptotic expansion for the return amplitude with $d = 2, \varepsilon = 1.9\,\gamma$, as is plotted in Fig. 3.6. The reason for this is again the appearance of a new resonance state at $\varepsilon = 2\,\gamma$.

And lastly, from Fig. 3.7 with $d = 10$, we again find that this result holds in general: Around $\varepsilon \in \{0.4\,\gamma, 3.6\,\gamma\}$, new resonance states appear, as can be seen in panel (e). Correspondingly, the convergence in (a) and (d) is quite poor. Whereas at $\varepsilon \in \{1.9\,\gamma, 2.5\,\gamma\}$, no new resonance states appear; and the associated plots (b) and (c) show much better accordance between the numerics and the asymptotic prediction.

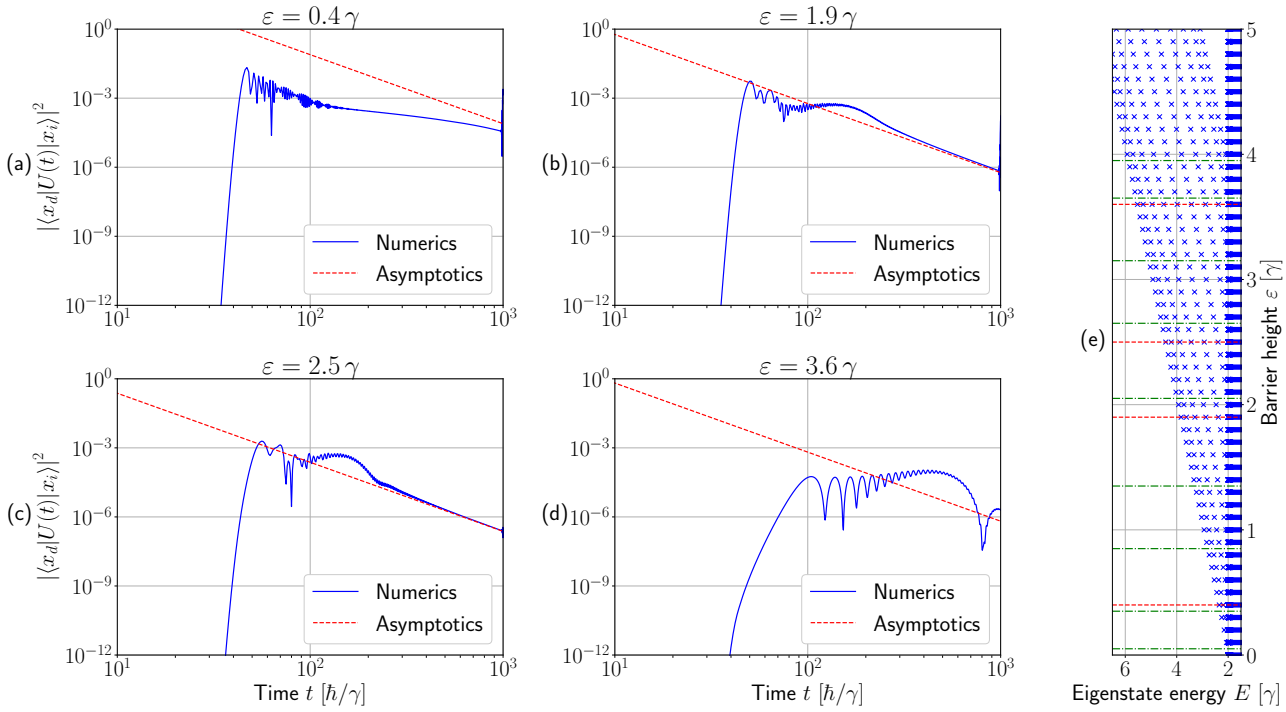

Figure 3.4: Double logarithmic plot of the transition amplitude $|\langle x_d|U(t)|x_i\rangle|^2$ for $d = 10, x_d = 50, x_i = -40$ and four different barrier heights ε. The amplitude is calculated numerically for a finite lattice with $N = 2000$ and compared to the asymptotic result (3.7); the residues of the transmission coefficient are thereby neglected since they cannot be calculated analytically for $d = 10$. In panel (e), we include an excerpt of Fig. 2.4 and highlight the four values of ε considered in (a) to (d) with a dashed line. In addition, the positions where new resonance states appear are indicated by dash-dotted lines. For $\varepsilon \in \{0.4\,\gamma, 3.6\,\gamma\}$, where new resonance states appear, the numerics does not converge to the asymptotic expansion within the considered time window. In contrast, no new resonance states appear for $\varepsilon \in \{1.9\,\gamma, 2.5\,\gamma\}$; and, correspondingly, the convergence is pretty good.

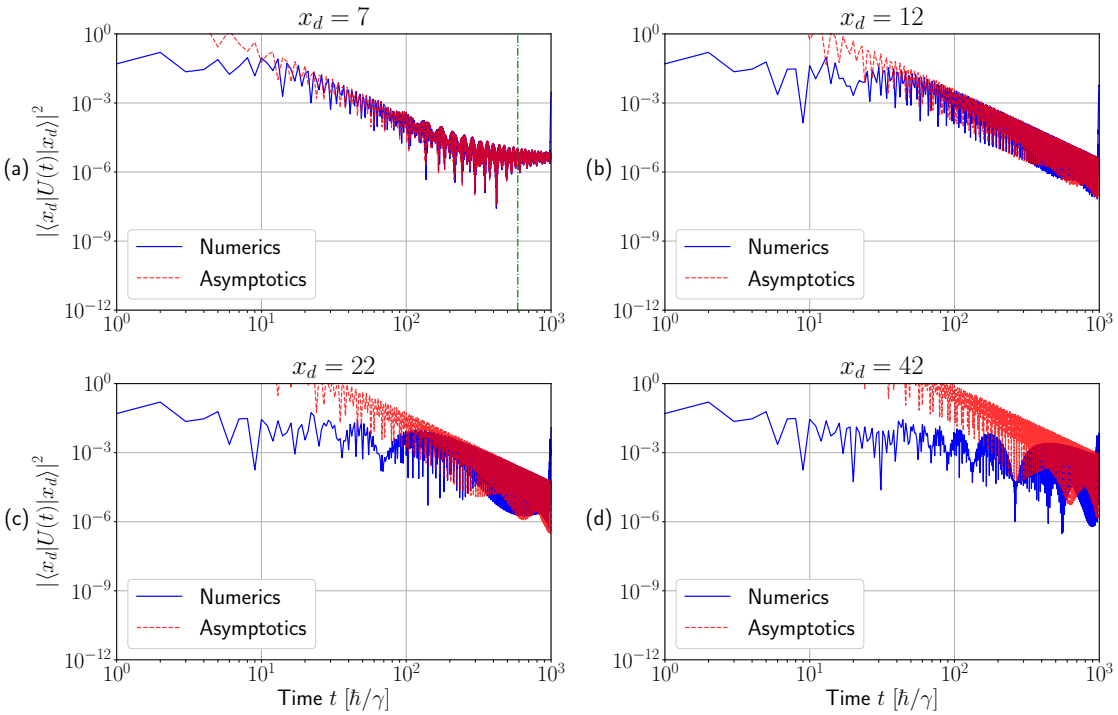

Figure 3.5: Double logarithmic plot of the return amplitude $|\langle x_d|U(t)|x_d\rangle|^2$ for $d = 2, \varepsilon = 2.5\,\gamma$ and four different detection sites x_d. The amplitude is calculated numerically for a finite lattice with $N = 2000$ and compared to the asymptotic result (3.10). In panels (a) and (b), the analytic expansion fits the simulation very well. In particular, we also find the transition from the power-law decay to the quasi-periodic function in plot (a), where we also marked $t_0^{\mathrm{R}} \sim x_d^{4/3}\, \mathrm{e}^{4\hat{\kappa} x_d/3}\, \hbar/\gamma$, according to Eq. (3.11), with a vertical line. With increasing x_d, however, we find in (c) and (d) that the convergence of the numerics to the asymptotic expansion is much slower.

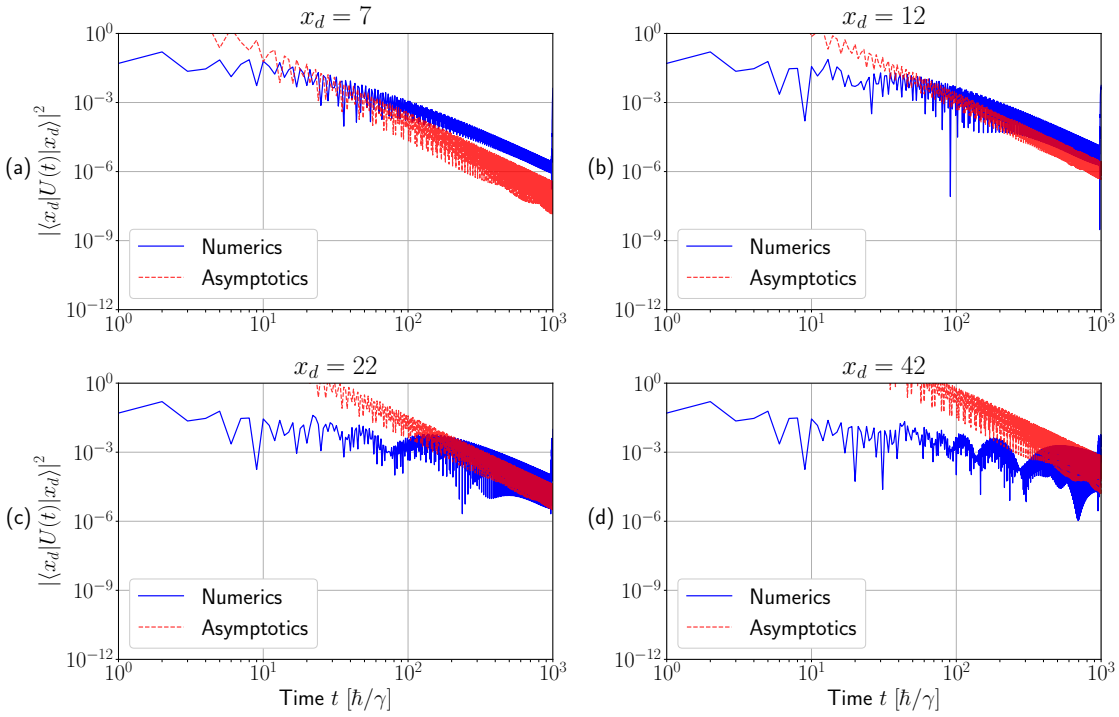

Figure 3.6: Double logarithmic plot of the return amplitude $|\langle x_d|U(t)|x_d\rangle|^2$ for $d = 2, \varepsilon = 1.9\,\gamma$ and the same four x_d as in Fig. 3.5. The amplitude is calculated numerically for a finite lattice with $N = 2000$ and compared to the asymptotic result (3.10). In contrast to Fig. 3.5, none of the four plotted numerical simulations converges to the asymptotic approximation within the considered time window. The reason for this is the different value of the barrier height ε.

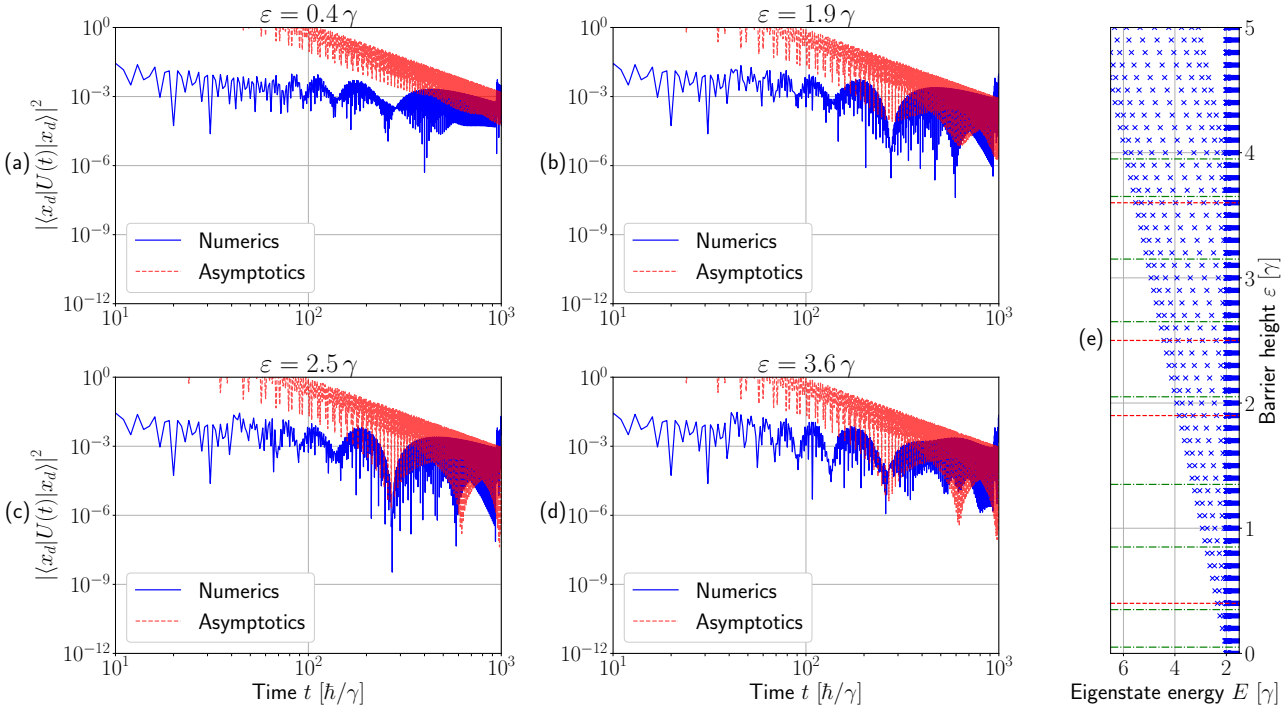

Figure 3.7: Double logarithmic plot of the return amplitude $|\langle x_d|U(t)|x_d\rangle|^2$ for $d = 10, x_d = 50$ and four different barrier heights ε. The amplitude is calculated numerically for a finite lattice with $N = 2000$ and compared to the asymptotic result (3.10); the residues of the transmission coefficient are thereby neglected since they cannot be calculated analytically for $d = 10$. In panel (e), we include an excerpt of Fig. 2.4 and highlight the four values of ε considered in (a) to (d) with a dashed line. In addition, the positions where new resonance states appear are indicated by dash-dotted lines. Similar to Fig. 3.4, we find that, for $\varepsilon \in \{0.4\,\gamma, 3.6\,\gamma\}$, where new resonance states appear, the convergence of the numerics to the asymptotic form is much worse than for $\varepsilon \in \{1.9\,\gamma, 2.5\,\gamma\}$, where no new resonance states appear.

Chapter 4

First detection statistics

4.1 Definitions and renewal equation

Using the results from the preceding sections, we will finally analyze the first detection probability F_n under stroboscopic projective measurements in this chapter. We start by recapitulating the actual problem to solve: Consider a particle which is at time $t = 0$ prepared in the position eigenstate $|x_i\rangle$ on the left side of the potential barrier (i.e. $x_i \leq -1$). Now, we let this particle evolve freely according to the Hamiltonian (2.2); but at discrete times $t \in \{\tau, 2\tau, ...\}$, we make projective measurements at the pre-defined detection site $|x_d\rangle$ on the right side of the barrier (i.e. $x_d \geq d$). These measurements are conducted using the projection operator $D := |x_d\rangle\langle x_d|$; and we use the standard von Neumann measurement, which implies the projection of the particle's state vector on $|x_d\rangle$ with subsequent renormalization [25]. With this setup, we ask for the probability F_n that the very first successful detection at x_d will occur at the nth measurement attempt (i.e. at $t = n\tau, n \in \mathbb{N}^+$).

To find this probability, we must analyze the particle's time evolution. Let $|\psi(t)\rangle$ denote the particle's wave function at time t, with $|\psi(0)\rangle = |x_i\rangle$. Before the first measurement at $t = \tau$, the particle evolves freely according to the unitary $U(t) = \mathrm{e}^{-\mathrm{i}\mathcal{H}t/\hbar}$. Hence, we get:

$$|\psi(\tau^-)\rangle = U(\tau)\,|x_i\rangle\,,$$

where the superscript $-$ $(+)$ denotes the moment right before (right after) the measurement attempt. The detection probability P_1 at the first measurement attempt is now given by

$$P_1 = |\langle x_d|U(\tau)|x_i\rangle|^2\,.$$

However, with probability $(1-P_1)$, the measurement is unsuccessful, the wave function vanishes at the detection site and is renormalized. The wave function right after the (unsuccessful) measurement is, then, given by

$$|\psi(\tau^+)\rangle = \frac{(1-D)\,U(\tau)\,|x_i\rangle}{\sqrt{1-P_1}}.$$

Between $\tau < t < 2\tau$, the particle again evolves according to the unitary. Thus, we

find, similarly to the above:

$$|\psi(2\tau^-)\rangle = \frac{U(\tau)\,(1-D)\,U(\tau)\,|x_i\rangle}{\sqrt{1-P_1}},$$
$$P_2 = \frac{\left|\langle x_d|U(\tau)\,(1-D)\,U(\tau)|x_i\rangle\right|^2}{1-P_1},$$
$$|\psi(2\tau^+)\rangle = \frac{(1-D)\,U(\tau)\,(1-D)\,U(\tau)\,|x_i\rangle}{\sqrt{1-P_2}\sqrt{1-P_1}}.$$

If we repeat this recursion process, we find that the detection probability P_n to find the particle at x_d at the nth measurement attempt is given by

$$P_n = \frac{\left|\langle x_d|U(\tau)\left((1-D)\,U(\tau)\right)^{n-1}|x_i\rangle\right|^2}{\prod_{j=1}^{n-1}\left(1-P_j\right)}.$$

However, we are not interested in P_n, which is the conditional probability of a successful detection at the nth measurement under the condition that all previous measurement attempts $j \in \{1,...,n-1\}$ were unsuccessful. Instead, we seek to find the joint probability F_n of successful detection at the nth attempt and unsuccessful measurement before. By the chain rule, this probability is given by

$$F_n = P_n \prod_{j=1}^{n-1}\left(1-P_j\right) = \left|\langle x_d|U(\tau)\left((1-D)\,U(\tau)\right)^{n-1}|x_i\rangle\right|^2,$$

and motivates the definition of the first detection amplitude φ_n:

$$\varphi_n := \langle x_d|U(\tau)\left((1-D)\,U(\tau)\right)^{n-1}|x_i\rangle \quad \Rightarrow \quad F_n = |\varphi_n|^2.$$

Based on these definitions, the authors of [23] derived a renewal equation for the amplitude φ_n by opening the binomial brackets $(...)^{n-1}$ in the above equation:

$$\varphi_n = \langle x_d|U(n\tau)|x_i\rangle - \sum_{j=1}^{n-1}\varphi_j\,\langle x_d|U((n-j)\tau)|x_d\rangle \tag{4.1}$$

In principle, this equation states that the first detection amplitude consists of two parts: First, it depends on the transition amplitude $\langle x_d|U(n\tau)|x_i\rangle$ that the particle propagated from $|x_i\rangle$ to $|x_d\rangle$ within time $t = n\tau$ and is detected there. On top, there is an interference with the amplitudes that the particle has already been detected at $|x_d\rangle$ previously, at time $t = j\tau$ (with $j \in \{1,2,...,n-1\}$), and then returned to $|x_d\rangle$ within the remaining time $(n-j)\tau$.

As mentioned in the introduction, this renewal equation (4.1) is our main tool to calculate the first detection probability F_n. We begin our investigation of the statistics of F_n by the analysis of some numerical results in the next section.

4.2 Analysis of numerical simulation

In this section, we present and analyze some numerical simulations of the first detection probability F_n. To compute F_n, we make use of the renewal equation (4.1) and of our previous finite-size numerical simulations of the unitary time evolution (see Sec. 3.4). Again, we must pay attention to finite-size effects which may appear for $t \gtrsim \hbar N/2\gamma$; thus, we will compute F_n only for $n \leq \hbar N/2\gamma\tau$ (where we used $t = n\tau$). We will mainly follow the approach of [24] in our present analysis.

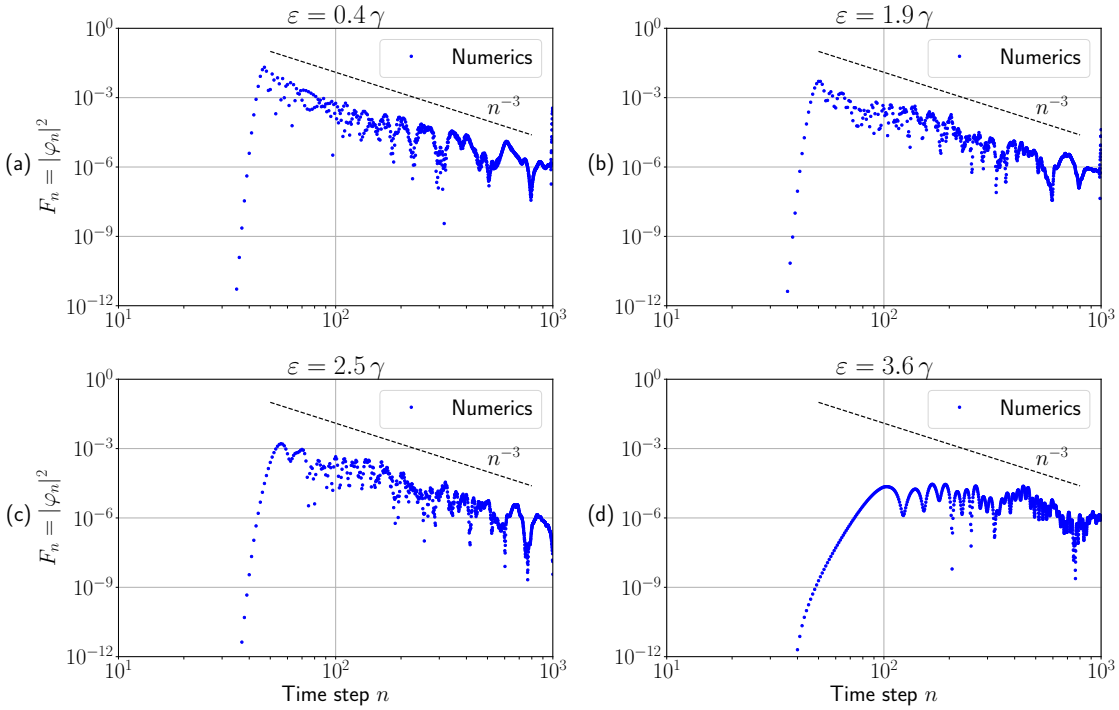

Figure 4.1: Double logarithmic plot of the first detection probability $F_n = |\varphi_n|^2$ for $d = 10, x_d = 50, x_i = -40, \tau = \hbar/\gamma$ and the same four barrier heights ε as in Fig. 3.4. The first detection probability is calculated numerically for a finite lattice with $N = 2000$. The straight dashed lines indicate an algebraic decay n^{-3}.

For the quantum walk without barrier, the authors of [24] found that F_n exhibits a monotonic increase up to its global maximum followed by a power-law decay proportional to n^{-3} with superimposed oscillations. Fig. 4.1 shows the numerically computed probabilities $F_n = |\varphi_n|^2$ for four different barrier heights ε with $N = 2000, d = 10, x_d = 50, x_i = -40, \tau = \hbar/\gamma$. It can be seen that the monotonic increase and power-law decay $F_n \propto n^{-3}$ also appear in our case, in the presence of a potential barrier. However, depending on the barrier height ε, the power-law decay does not begin immediately after the first local maximum of F_n but only at much later times, as can be seen in chart (d). Moreover, while the F_n indeed show superimposed oscillations, these oscillations do not feature a single distinct frequency, in contrast to the results of [24]. These findings are equally valid for simulations with a larger lattice $N = 10000$ and many further barrier heights $\varepsilon \in \{0.1\,\gamma, 0.2\,\gamma, ..., 5.0\,\gamma\}$.

In the next step, we study the probabilities F_n for the Hartman effect that we mentioned in the introduction. For this, we take the F_n curves for different barrier heights ε and determine their characteristic attributes. Since F_n is, obviously, not a

symmetric probability distribution, it is expected that its mean value and the global maximum (also called the mode) do not coincide; quite the contrary, we expect a very different behavior of the mean and the mode because F_n exhibits a power-law decay (i.e. a very slow decay, compared to exponential, that can lead to a very large mean value). As mentioned above, on the infinite line without barrier, the global maximum is also the very first local maximum and is determined by the maximum group velocity on the lattice [24], which is $v_{\mathrm{g,\,max}} = 2\gamma/\hbar$ as mentioned in Sec. 3.4. However, as we found in Fig. 4.1, the very first maximum is not always the global maximum in the presence of a barrier. Hence, in our analysis, we will consider seperately the position of the global maximum $t_{\max} = \tau n_{\max}$ and of the very first maximum $t_{\mathrm{inc}} = \tau n_{\mathrm{inc}}$ (where n_{inc} is the smallest n such that $F_{n+1} < F_n$), which is also called the incidence time. Since these quantities are related to the group velocity of the particle's wave function [24], it is expected that due to the Hartman effect $t_{\max}$ and t_{inc} may be shifted to smaller values depending on the barrier height ε. Furthermore, we compute the mean first detection time $\langle T \rangle$ from our F_n curves, and investigate whether the tunnel effect causes a temporal shift in the average first detection statistics as well. Logically, we cannot calculate the mean exactly using finite-size simulations; instead, we estimate it by

$$\langle T \rangle \approx \frac{\tau \sum_{n=1}^{0.9\cdot\hbar N/2\gamma\tau} n \cdot F_n}{\sum_{n=1}^{0.9\cdot\hbar N/2\gamma\tau} F_n},$$

whereby we only consider the values F_n up to $n = 0.9 \cdot \hbar N/2\gamma\tau$ to reliably exclude any finite-size effects. Similarly, we also find an estimated total detection probability:

$$P_{\mathrm{det}} \approx \sum_{n=1}^{0.9\cdot\hbar N/2\gamma\tau} F_n.$$

If the first detection probability followed a monotonic power-law decay $F_n \propto n^{-3}$, the last (and thus also least) summand in the two above equations might serve as an estimate of the error we make by truncating the sums at $n = 0.9 \cdot \hbar N/2\gamma\tau$. However, because of the superimposed oscillations, F_n does not decay monotonically; hence, we need a more sophisticated estimation of the convergence error. For this, we sum up the terms for $n = 0.8...0.9 \cdot \hbar N/2\gamma\tau$ to average out the phases of the superimposed complex oscillations and divide the resulting sum by the total estimated value. This way, we get an estimation of the relative convergence error:

$$r_{P_{\mathrm{det}}} \approx \frac{\sum_{n=0.8\cdot\hbar N/2\gamma\tau}^{0.9\cdot\hbar N/2\gamma\tau} F_n}{P_{\mathrm{det}}},$$
$$r_{\langle T \rangle} \approx \frac{\tau \sum_{n=0.8\cdot\hbar N/2\gamma\tau}^{0.9\cdot\hbar N/2\gamma\tau} n \cdot F_n}{\langle T \rangle} + r_{P_{\mathrm{det}}}.$$

Since the relative errors of P_{det} and $\sum_{n=0}^{0.9\cdot\hbar N/2\gamma\tau} n \cdot F_n$ originate solely from the truncation of the sum, we assume them to be fully correlated. Hence, they are added together to get $r_{\langle T \rangle}$ (instead of quadratic addition).

The results are shown in Fig. 4.2. The relative errors $r_{\langle T \rangle}, r_{P_{\mathrm{det}}}$ are drawn as error bars in both directions; $r_{P_{\mathrm{det}}}$ is, however, not visible because the values are too small. We first inspect the detection probability which, for $\varepsilon < 4\,\gamma$, slowly decreases as the

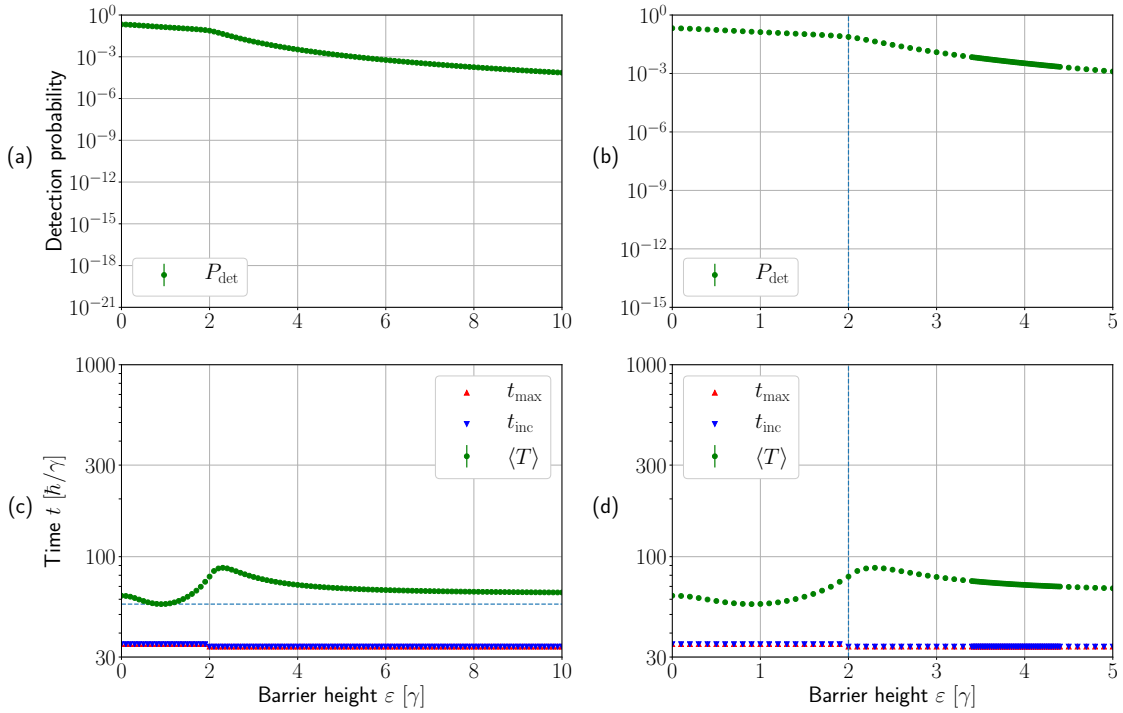

Figure 4.2: Semi-logarithmic plots of the first detection probability's characteristic attributes for $d = 10, x_d = 42, x_i = -32, \tau = \hbar/\gamma$ and different barrier heights $\varepsilon \in \{0.0\,\gamma, 0.1\,\gamma, ..., 10.0\,\gamma\}$. Panels (b) and (d) zoom into the interval $\varepsilon = 0...5\,\gamma$ with a finer sampling in the sector $\varepsilon \in \{3.4\,\gamma, 3.425\,\gamma, ..., 4.4\,\gamma\}$. Additionally, (d) includes vertical lines at those barrier heights ε where the number of resonance states B increases (as observed in the ε-dependence of the spectrum in Fig. 2.4). In (b), only the emergence of the last resonance state is indicated by a vertical line. The horizontal line in (c) marks the global minimum of $\langle T \rangle$. The estimated relative errors $r_{\langle T \rangle}, r_{P_{\mathrm{det}}}$ are shown as error bars; $r_{P_{\mathrm{det}}}$ is not visible, though, because the values are too small.

barrier becomes higher, as can be seen in plots (a) and (b). At about the barrier height where the last new resonance state arises (vertical line in plot (b)), the detection probability suddenly drops. After this point, the barrier is opaque and the particle can only overcome the barrier by quantum tunneling, which explains the rapid decrease for larger ε. The probabilities at the incidence maximum, $F_{n_{\mathrm{inc}}}$, and at the global maximum, $F_{n_{\mathrm{max}}}$, very much follow the behavior of P_{det}, but naturally at values which are suppressed by one to two orders of magnitude. For brevity, we excluded them from Fig. 4.2 since they do not provide any additional information.

The first thing we notice in panels (c) and (d) is that t_{inc} and t_{max} appear discretized for some ε. Naturally, they are not really discretized but we can understand what is causing this issue by taking a look at Fig. 4.1 again. Especially in panel (d), we can see that F_n exhibits many local maxima that may have almost the same height when varying ε. Consequently, the position of the global maximum of F_n is discontinuous when one of these local maxima exceeds the height of the former global maximum. Similarly, new maxima may appear at any position within the F_n curve when we vary the barrier height ε. If such a new maximum appears at $t < t_{\mathrm{inc}}$, then t_{inc} is discontinuous. These two effects cause the discontinuities that are visible in Fig. 4.2.

The mean value $\langle T \rangle$ is, naturally, not affected much by these effects because it is a global property of the probability distribution; thus, no discontinuities are visible in the corresponding graphs.

For $\varepsilon < 3.5\,\gamma$, the incidence maximum of F_n is also the global maximum (i.e. $t_{\text{inc}} = t_{\max}$), as we have already seen in Fig. 4.1. While t_{inc} and $t_{\max}$ increase monotonically for $0 < \varepsilon < 3.5\,\gamma$, the mean value $\langle T \rangle$ has a cascade-like shape which can be seen especially in chart (d) in Fig. 4.2. In plot (d), we also included a vertical line between neighboring ε where the number of resonance states B increases (according to the energy spectrum in Fig. 2.4). From these, we can see that the cascades follow the emergence of new resonance states: $\langle T \rangle$ has a local maximum around the value ε where a new resonance state arises. Apart from this cascade-like substructure, $\langle T \rangle$ generally also increases from $0.5\,\gamma < \varepsilon < 3.5\,\gamma$. Only for very small barrier heights $0 < \varepsilon < 0.5\,\gamma$, $\langle T \rangle$ contrarily decreases as ε gets larger, and features a global minimum around $\varepsilon \approx 0.5\,\gamma$.

For $\varepsilon \lessapprox 4\,\gamma$, we find the global maximum of t_{inc}, $t_{\max}$ and $\langle T \rangle$. From the vertical lines, we see that the maxima of $t_{\max}$ and $\langle T \rangle$ lie exactly at the value of ε where the last resonance state emerges (the 10th state, in this case, $d = 10$), which is also where the barrier becomes (almost) opaque. The maximum of t_{inc} is located at a slightly lower ε. Unfortunately, we cannot determine whether any of the considered maxima diverges around this point because our limited numerical calculation always yields finite results. (In particular, the values are always smaller than $\hbar N/2\gamma\tau$ because of the finite size of the simulated lattice.)

Lastly, we take a closer look at large barrier heights $\varepsilon > 4\,\gamma$. As we can see in plot (a), the tunneling probability decreases with increasing barrier height, which is exactly what we expect from quantum tunneling. In particular, the probability of detecting the particle at all behind the barrier quickly becomes ridiculously improbable with $P_{\text{det}} \ll 10^{-9}$. In (c), we further find that t_{inc} and $t_{\max}$ decrease as well and finally are equal again for very large barriers. Especially notable is that they become smaller than for $\varepsilon = 0$, where they are around $t_{\text{inc}} = t_{\max} \approx 40\,\hbar/\gamma$. As the authors of [24] pointed out for the case without potential barrier, the incidence time t_{inc} corresponds to the part of the particle wave which has the maximum group velocity. The shift of t_{inc} we observe therefore implies that the tunnel effect causes an apparent increase in the group velocity underneath the barrier. This interpretation is, however, not quite correct. In the barrier region, the wave vector k of the particle is complex; consequently, the group velocity, which is defined by $\mathrm{d}E/\,\mathrm{d}k$, is also complex-valued. Now, while the modulus of this complex group velocity indeed becomes larger than $v_{\mathrm{g},\max} = 2\gamma/\hbar$ (which is the maximum group velocity outside the barrier as mentioned in Sec. 3.4), it still lacks comparability to its real-valued counterpart outside the barrier. Nonetheless, we find that the tunneling process itself seems to be almost instantaneous; hence, we recovered a manifestation of the Hartman effect. The estimated mean first detection time $\langle T \rangle$ also decreases for higher barriers, though much slower than t_{inc} and $t_{\max}$. It eventually also becomes smaller than its value without barrier (which is $\langle T \rangle \approx 70\,\hbar/\gamma$); however, its global minimum, which is marked with a horizontal line in chart (c), lies at $\varepsilon \approx 0.6\,\gamma$ (with $\langle T \rangle \approx 57\,\hbar/\gamma$) and not at $\varepsilon \to \infty$. (We verified that this holds for $\varepsilon \leq 10000\,\gamma$ within our numerical accuracy.)

The results discussed above were equally verified for $d = 9$ and $\tau = 0.5 \cdot \hbar/\gamma$.

4.3 Analytic ansatz

In this last section, we present an ansatz to calculate the first detection amplitude φ_n and probability F_n analytically from the unitary time evolution that we considered in Chapters 2 and 3. The central tool to accomplish this is again the renewal equation (4.1). It relates the first detection amplitude φ_n recursively to the transition and return amplitude $\langle x_d|U(n\tau)|x_i\rangle$, $\langle x_d|U(n\tau)|x_d\rangle$, respectively, which we computed in Chapter 3. In particular, we seek to analytically derive the $F_n \propto n^{-3}$ and $\varphi_n \propto n^{-3/2}$ proportionalities in the limit $n \to \infty$. For this, we notice that for a fixed measurement interval τ, the limits $n \to \infty$ and $t = n\tau \to \infty$ are obviously equivalent. Hence, we begin by inserting $t = n\tau$ into Eqs. (3.7) and (3.10) to get the desired form of the transition and return amplitude in the limit $n \to \infty$, which we will call v_n and u_n from now on:

$$\begin{aligned} u_n &:= \langle x_d|U(n\tau)|x_d\rangle \overset{n\to\infty}{\sim} \frac{1}{n^{3/2}}\left(C_+ \mathrm{e}^{\mathrm{i}\Lambda n} + C_- \mathrm{e}^{-\mathrm{i}\Lambda n}\right) + \sum_{l=1}^{B} \left|\langle \psi_{\kappa_l}|x_d\rangle\right|^2 \mathrm{e}^{-\mathrm{i}\Lambda_l n}, \\ v_n &:= \langle x_d|U(n\tau)|x_i\rangle \overset{n\to\infty}{\sim} \frac{1}{n^{3/2}}\left(D_+ \mathrm{e}^{\mathrm{i}\Lambda n} + D_- \mathrm{e}^{-\mathrm{i}\Lambda n}\right) + \sum_{l=1}^{B} \langle x_d|\psi_{\kappa_l}\rangle \langle \psi_{\kappa_l}|x_i\rangle \mathrm{e}^{-\mathrm{i}\Lambda_l n}, \end{aligned} \tag{4.2}$$

where we introduced the following abbreviations:

$$\begin{aligned} \Lambda &:= \frac{2\gamma\tau}{\hbar}, & \Lambda_l &:= \frac{E_l\tau}{\hbar}, \\ C_+ &:= \frac{\mathrm{e}^{-3\mathrm{i}\pi/4}}{8\sqrt{\pi(\gamma\tau/\hbar)^3}}\,\mathcal{R}_{x_d}(0), & C_- &:= \frac{\mathrm{e}^{3\mathrm{i}\pi/4}}{8\sqrt{\pi(\gamma\tau/\hbar)^3}}\,\mathcal{R}_{x_d}(\pi), \\ D_+ &:= \frac{\mathrm{e}^{-3\mathrm{i}\pi/4}}{8\sqrt{\pi(\gamma\tau/\hbar)^3}}\,\mathcal{T}_{\xi}(0), & D_- &:= \frac{\mathrm{e}^{3\mathrm{i}\pi/4}}{8\sqrt{\pi(\gamma\tau/\hbar)^3}}\,\mathcal{T}_{\xi}(0)\,(-1)^{\xi}. \end{aligned}$$

Originating from the renewal equation, the authors of [21] derived a very general connection between u_n, v_n and φ_n by analyzing the branch points of their respective generating functions (e.g. $\varphi(z) := \sum_{n=0}^{\infty} \varphi_n z^n$). In particular, they found that if $u_n \propto n^{-3/2}$ and $v_n \propto n^{-3/2}$, then the first detection amplitude is also $\varphi_n \propto n^{-3/2}$ and the coefficients are related as follows [21, Appendix C]:

$$\varphi_n \overset{n\to\infty}{\sim} \frac{1}{n^{3/2}}\left(J_+ \mathrm{e}^{\mathrm{i}\Lambda n} + J_- \mathrm{e}^{-\mathrm{i}\Lambda n}\right), \qquad J_\pm = \frac{u(\mathrm{e}^{\mp\mathrm{i}\Lambda})D_\pm - v(\mathrm{e}^{\mp\mathrm{i}\Lambda})C_\pm}{\left(u(\mathrm{e}^{\mp\mathrm{i}\Lambda})\right)^2}, \tag{4.3}$$

where $u(\mathrm{e}^{\mp\mathrm{i}\Lambda}) = \sum_{n=0}^{\infty} u_n \mathrm{e}^{\mp\mathrm{i}\Lambda n}$, and analogously for $v(\mathrm{e}^{\mp\mathrm{i}\Lambda})$. However, their results are limited to Hamiltonians with a completely continuous spectrum only, whereas the Hamiltonian considered also features discrete resonance states. Hence, the result from [21] is technically not applicable for us; which is also obvious from the above Eq. (4.2), where we see that, in our case, u_n and v_n do not purely follow a power-law decay but also contain a quasi-periodic function (i.e. $\sum_l ...\mathrm{e}^{-\mathrm{i}\Lambda_l n}$), which originates from the discrete part of the spectrum, as mentioned in Chapter 3.

Nonetheless, we will briefly compute the coefficients $J_\pm$ according to Eq. (4.3) and compare the resulting first detection amplitudes φ_n to our numerical simulation. For

this, we also need to calculate the values $u(\mathrm{e}^{\mp \mathrm{i}\Lambda})$, $v(\mathrm{e}^{\mp \mathrm{i}\Lambda})$ which enter the expression for $J_\pm$. To get these, we insert our numerically computed transition and return amplitudes into the generating function definition, but only sum up to $n = 0.9 \cdot \hbar N/2\gamma\tau$ to reliably exclude any finite-size effects (like we did in the last section for P_{det} and $\langle T \rangle$):

$$u(\mathrm{e}^{\mp \mathrm{i}\Lambda}) \approx \sum_{n=0}^{0.9\cdot\hbar N/2\gamma\tau} u_n \mathrm{e}^{\mp \mathrm{i}\Lambda n}, \qquad v(\mathrm{e}^{\mp \mathrm{i}\Lambda}) \approx \sum_{n=0}^{0.9\cdot\hbar N/2\gamma\tau} v_n \mathrm{e}^{\mp \mathrm{i}\Lambda n}$$

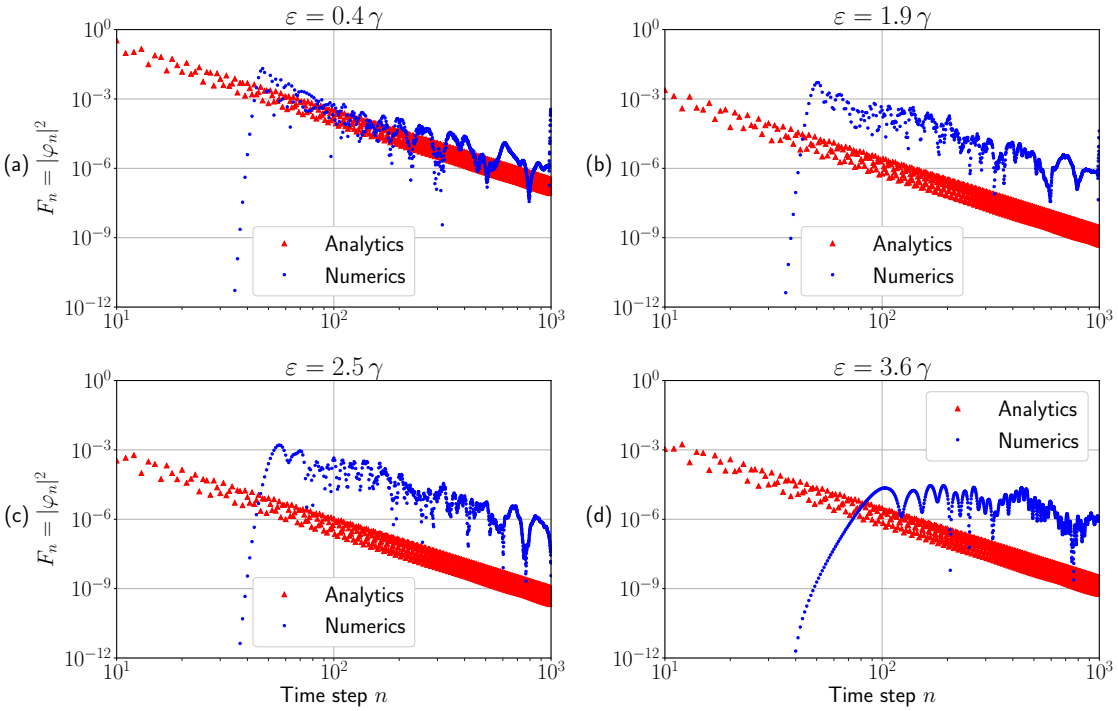

Figure 4.3: Double logarithmic plot of the first detection probability $F_n = |\varphi_n|^2$ for $d = 10, x_d = 50, x_i = -40, \tau = \hbar/\gamma$ and the same four barrier heights ε as in Fig. 3.4. The detection probability is calculated numerically for a finite lattice with $N = 2000$ and compared to the analytical result (4.3).

In Fig. 4.3, we plot $F_n = |\varphi_n|^2$ for four different barrier heights ε with $N = 2000, d = 10, x_d = 50, x_i = -40, \tau = \hbar/\gamma$. We see that our analytic approximation does not fit the numerical simulation. Apart from plot (a), the prediction even differs by two to three orders of magnitude from the simulated data. Regarding this result, we must take a look at the main sources of error in our analytical considerations.

The first source of error to consider is the poor convergence we found for the transition and return amplitude near those values of ε where new resonance states emerge (see Sec. 3.4). However, the discrepancy in Fig. 4.3 does not seem to coincide with the slow convergence we found for $\varepsilon \in \{0.4\,\gamma, 3.6\,\gamma\}$ in Figs. 3.4 and 3.7; quite the contrary, our analytic F_n curves for $\varepsilon \in \{1.9\,\gamma, 2.5\,\gamma\}$ apparently differ most from the numerics. Hence, this is certainly not the primary source of error.

Next, we take a look at the convergence of the values $u(\mathrm{e}^{\mp \mathrm{i}\Lambda})$, $v(\mathrm{e}^{\mp \mathrm{i}\Lambda})$ and, correspondingly, $J_\pm$. For this, we sum the terms for $n = 0.8...0.9 \cdot \hbar N/2\gamma\tau$ (like in the last

section) as a rough estimate of the convergence error:

$$r_{u(\mathrm{e}^{\mp \mathrm{i}\Lambda})} \approx \left| \frac{\sum_{n=0.8\cdot\hbar N/2\gamma\tau}^{0.9\cdot\hbar N/2\gamma\tau} u_n \mathrm{e}^{\mp \mathrm{i}\Lambda n}}{u(\mathrm{e}^{\mp \mathrm{i}\Lambda})} \right|, \qquad r_{v(\mathrm{e}^{\mp \mathrm{i}\Lambda})} \approx \left| \frac{\sum_{n=0.8\cdot\hbar N/2\gamma\tau}^{0.9\cdot\hbar N/2\gamma\tau} v_n \mathrm{e}^{\mp \mathrm{i}\Lambda n}}{v(\mathrm{e}^{\mp \mathrm{i}\Lambda})} \right|$$

From these relative errors, we estimate the relative errors of $J_\pm$ by the Gaussian propagation of uncertainty, whereby we, however, only consider the modulus of all complex-valued quantities:

$$r_{J_\pm} = \frac{1}{|J_\pm|} \sqrt{\left| r_{u(\mathrm{e}^{\mp \mathrm{i}\Lambda})} \cdot u(\mathrm{e}^{\mp \mathrm{i}\Lambda}) \cdot \frac{\partial J_\pm}{\partial u(\mathrm{e}^{\mp \mathrm{i}\Lambda})} \right|^2 + \left| r_{v(\mathrm{e}^{\mp \mathrm{i}\Lambda})} \cdot v(\mathrm{e}^{\mp \mathrm{i}\Lambda}) \cdot \frac{\partial J_\pm}{\partial v(\mathrm{e}^{\mp \mathrm{i}\Lambda})} \right|^2}$$

For the four values of ε considered in Fig. 4.3, we find relative errors of $r_{J_\pm} < 0.12$. This seems pretty much at first; in particular, considering that the relative error of F_n is twice the relative error of φ_n, and, moreover, the two errors may eventually add up depending on the phase of $\mathrm{e}^{\pm \mathrm{i}\Lambda n}$. But even a relative error of ≈ 0.5 on the analytic F_n curves would not suffice to explain the deviation of one to three orders of magnitude from the numerical simulation.

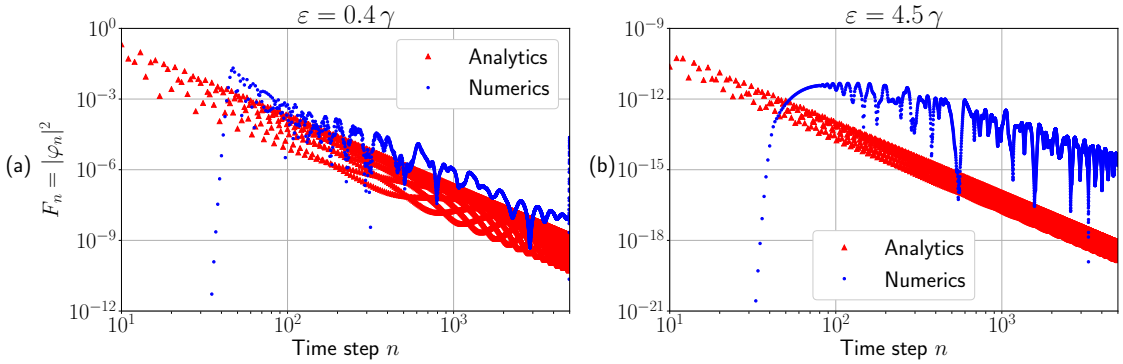

Figure 4.4: Double logarithmic plot of the first detection probability $F_n = |\varphi_n|^2$ for $d = 10, x_d = 50, x_i = -40, \tau = \hbar/\gamma$ and two different barrier heights ε. The detection probability is calculated numerically for a finite lattice with $N = 10000$ and compared to the analytic result (4.3).

To underpin the latter statement, we also plot F_n for two barrier heights ε for a much larger lattice with $N = 10000$ (and, as before, $d = 10, x_d = 50, x_i = -40, \tau = \hbar/\gamma$). The result is shown in Fig. 4.4. A comparison of panels (a) from Figs. 4.3 and 4.4 shows a slight difference between the two analytic curves. This implies that the values $J_\pm$ are indeed (slightly) changed now that $u(\mathrm{e}^{\mp \mathrm{i}\Lambda})$ and $v(\mathrm{e}^{\mp \mathrm{i}\Lambda})$ are calculated with much more summands. Nonetheless, the absolute deviation between the analytic and the numerical data is still about one order of magnitude like before. Thus, this error is, as far as we can tell by now, probably also not the dominant one.

Finally, the third 'source of error' is the discrete part of our energy spectrum, i.e. the resonance states, which we neglected by applying the results from [21]. However, we see from plot (b) in Fig. 4.4 that choosing a much larger ε does not reduce the discrepancy either, even though the terms associated with the resonance states decrease

with increasing barrier height ε.[1]

These results are further confirmed by simulations for different barrier widths $d \in \{1, 2\}$ and many more barrier heights ε (for $N \in \{2000, 10000\}$). Since we did not find a correlation between the discrepancy and the different parameter values, we do not include any further plots for these cases.

This result is naturally not unexpected given the fact that the approach to calculate the first detection amplitude φ_n from [21] is limited to completely continuous energy spectra. The main problem, which appears in their approach if the spectrum has a discrete part, is that the generating function $\varphi(z)$ acquires a pole at some $|z| > 1$ per (non-degenerate) discrete energy state. Thereby, the procedure of [21] to calculate φ_n becomes invalid. In a very recent work, the authors of [32] show that each discrete state contributes an exponential term $\mathrm{e}^{-\lambda n}, \mathrm{Re}(\lambda) > 0$ to the first detection amplitude φ_n (for $n \to \infty$), in case the spectrum is completely discrete. It seems reasonable to assume that, in our case of a mixed energy spectrum, the true φ_n will be a sum of a power-law term associated with the continuous part and a number of exponential functions corresponding to the discrete energy states; similar to the u_n and v_n in Eq. (4.2). In particular, the large deviation we found between our analytic consideration and our numerics suggests that the discrete energy states have a significant impact on the coefficients of the power-law term.

[1] The terms associated with the resonance states are proportional to $\langle \psi_{\kappa_l} | x_d \rangle \propto \mathrm{e}^{-\kappa_l x_d}$ and $\langle \psi_{\kappa_l} | x_i \rangle \propto \mathrm{e}^{-\kappa_l x_i}$, respectively. Together with $\kappa_l \propto \mathrm{arcosh}(E_l) \sim \mathrm{arcosh}(\varepsilon)$ according to Eq. (2.4) and Fig. 2.4, this gives a proportionality to $\mathrm{e}^{-\,\mathrm{arcosh}(\varepsilon)}$.

Chapter 5

Discussion and summary

Even though the phenomenon of quantum tunneling has continuously been of great interest since the development of quantum mechanics, the question of how much time a particle requires to penetrate a barrier remains controversial until today. This is mainly due to two general misconceptions: First, quantum mechanics does not allow the existence of a time-of-arrival operator [3]; and second, a quantum particle does not possess a trajectory in the classical sense, but its position and momentum can only be found by a measurement process, which, in turn, inevitably alters the particle's behavior. As a consequence, there cannot be an intrinsic definition of the tunneling time but only an operational one, which directly leads to the problem that different theoretical and experimental approaches yield different results.

To overcome these issues, we based our analysis of the tunnel effect on the theory of the quantum walk. While the classical random walk has been well-studied for more than one century, the quantum walk was only introduced in the 90s by [15]. Similar to quantum tunneling, the first arrival time of a continuous-time quantum walker is also undefined. Nevertheless, considering the effort put into the development of quantum computers, it is high time for this issue to be solved because it is closely related to the quantum search problem [21].

To address these issues, we analyzed the tunnel effect on a one-dimensional infinite line of discrete lattice points and with a rectangular potential barrier. Thereby, we studied a particle that is initially located at some lattice site x_i and evolves freely according to the Schrödinger equation. Following [22, 23, 24], we resolved the lack of a time-of-arrival operator by implementing a series of repeated projective measurements at a pre-defined detection site x_d with a fixed measurement interval τ. This way, we translated the undefined arrival time problem into a precisely defined detection problem based on the standard von Neumann measurement theory [25]. The main challenge was to find the probability F_n that the very first successful detection occurs at the nth measurement attempt at time $t = n\tau$. Our central tool to accomplish this was the renewal equation (4.1) derived by [23], which recursively reduces the calculation of F_n to the unitary time evolution in the absence any measurement.

In Chapter 2, we started our analysis by defining the tight-binding Hamiltonian with coupling strength γ including a rectangular potential barrier of width d (measured as a dimensionless number of lattice sites) and height ε. Using the stationary wave ansatz, we found that the associated energy spectrum consists of a continuous part with eigenvalues in the energy band $-2\gamma \leq E \leq 2\gamma$, similar to the free propagation [24]; and additionally a number of $B \leq d$ discrete resonance states with $E > 2\gamma$ depending on d

and ε (see Fig. 2.4). Similar to other scattering problems [26, p. 13.13], the resonance states are determined by the poles of the reflection and transmission coefficient (see Eqs. (2.6), (2.7) and (2.13)), which allows for a convenient calculation of their overlap with specific position eigenstates (see Eq. (2.21)).

In Chapter 3, we calculated the transition amplitude $\langle x_d|U(t)|x_i\rangle$ and return amplitude $\langle x_d|U(t)|x_d\rangle$ using the spectral decomposition of the unitary time evolution operator. Using the method of steepest descents [30], we found the leading order asymptotic approximation of the amplitudes for large times $t \to \infty$ (see Eqs. (3.7) and (3.10)). We found that for $t \gg \hbar\xi/2\gamma$ (where $\xi = x_d - x_i$), the transition amplitude is given by two contributions. The transmission through the band states yields a power-law decay $t^{-3/2}$ with superimposed oscillations of frequency $\pm 2\gamma/\hbar$, which dominates at first. Beyond $t \gtrsim t_0^{\mathrm{T}}$ (defined by Eq. (3.8)), however, a quasi-periodic function governs the transition amplitude. This term originates from the resonance states. The same results also hold for the return amplitude. For $t \gg \hbar x_d/\gamma$, it is first dominated by a power-law decay $t^{-3/2}$ with again superimposed oscillations of frequency $\pm 2\gamma/\hbar$, which originates from the band states. And beyond a different $t \gtrsim t_0^{\mathrm{R}}$ (according to Eq. (3.11)), the resonance states dominate the return amplitude in form of a quasi-periodic function. These asymptotic results were verified by numerical simulation for a finite lattice. However, we found that the convergence significantly depends on ε. Around those values ε where the number of resonance states changes (see Figs. 3.4 and 3.7), the amplitudes converge much slower to their respective asymptotic forms than at other ε. Moreover, we stress again that the convergence also becomes much slower as x_d and x_i are moved further away from the barrier. This lack of accuracy could be overcome in future work by a more sophisticated steepest descents approximation with a different choice of the exponent function $f(k)$ that takes into account those poles of the transmission and reflection coefficient which lie close to the real axis (see Eqs. (3.3) and (3.9)).

In Chapter 4, we finally applied the results for the unitary time evolution to the original issue including the stroboscopic projective measurements. Using the renewal equation (4.1) from [23], we numerically computed the first detection probability F_n and analyzed it following the studies of [24] for the quantum walker without barrier. Similar to their results, we found that F_n also exhibits a monotonic increase followed by an oscillatory decay with an envelope proportional to n^{-3} in the presence of a potential barrier. However, depending on the barrier height ε, the power-law decay does not begin immediately after the first local maximum of F_n, but only at much later times (see Fig. 4.1). Furthermore, we investigated the position t_{inc} of the first local maximum of F_n (i.e. the incidence time) and the position $t_{\max}$ of its global maximum for a temporal shift depending on ε as suggested by the Hartman effect. We found that t_{inc} and $t_{\max}$ often coincide, as in the case without potential barrier [24], and, indeed, become smaller with increasing barrier height when the barrier is opaque (i.e. $\varepsilon \gtrsim 4\,\gamma$). They even get smaller than their values without barrier. We found the same behavior also for the mean first detection time $\langle T\rangle$ for $\varepsilon \gtrsim 4\,\gamma$, although we found its global minimum located around $\varepsilon \approx 0.5\,\gamma$ and not at $\varepsilon \to \infty$.

Lastly, we presented an analytic ansatz to calculate F_n following [21], assuming that the quasi-periodic terms that come from the resonance states were negligible (see Eqs. (4.2) and (4.3)). By comparison to the finite-size numerical simulation, however, we found that they must indeed not be neglected. It remains open for the future to combine the results of [21], where Hamiltonians with strictly continuous spectra

were considered, with the very recent work [32], where the completely discrete case is studied, to also find an analytic expression of the first detection probability for mixed spectra such as the one considered in this thesis.

Bibliography

[1] A. Enders and G. Nimtz. "On superluminal barrier traversal". *Journal de Physique I, 1693* (1992).

[2] G. Gamow. "Zur Quantentheorie des Atomkernes". *Zeitschrift für Physik 51, 204* (1928).

[3] G. R. Allcock. "The time of arrival in quantum mechanics". *Annals of Physics 53, 253* (1969).

[4] E. P. Wigner. "Lower Limit for the Energy Derivative of the Scattering Phase Shift". *Physical Review 98, 145* (1955).

[5] F. T. Smith. "Lifetime Matrix in Collision Theory". *Physical Review 118, 349* (1960).

[6] E. H. Hauge and J. A. Støvneng. "Tunneling times: a critical review". *Reviews of Modern Physics 61, 917* (1989).

[7] R. Landauer and T. Martin. "Barrier interaction time in tunneling". *Reviews of Modern Physics 66, 217* (1994).

[8] D. Sokolovski and L. M. Baskin. "Traversal time in quantum scattering". *Physical Review A 36, 4604* (1987).

[9] C. A. A. de Carvalho and H. M. Nussenzveig. "Time delay". *Physics Reports 364, 83* (2002).

[10] T. E. Hartman. "Tunneling of a Wave Packet". *Journal of Applied Physics 33, 3427* (1962).

[11] H. Aichmann and G. Nimtz. "On the Traversal Time of Barriers". *Foundations of Physics 44, 678* (2014).

[12] A. M. Steinberg, P. G. Kwiat, and R. Y. Chiao. "Measurement of the Single-Photon Tunneling Time". *Physical Review Letters 71, 708* (1993).

[13] U. S. Sainadh et al. "Attosecond angular streaking and tunneling time in atomic hydrogen". *Nature 568, 75* (2019).

[14] A. S. Landsman et al. "Ultrafast resolution of tunneling delay time". *Optica 1, 343* (2014).

[15] Y. Aharonov, L. Davidovich, and N. Zagury. "Quantum random walks". *Physical Review A 48, 1687* (1993).

[16] E. Farhi and S. Gutmann. "Quantum computation and decision trees". *Physical Review A 58, 915* (1998).

[17] J. Klafter and I. M. Sokolov. *First Steps in Random Walks*. Oxford University Press, 2011.

[18] M. Karski et al. “Quantum Walk in Position Space with Single Optically Trapped Atoms”. *Science 325, 174* (2009).

[19] H. B. Perets et al. “Realization of Quantum Walks with Negligible Decoherence in Waveguide Lattices”. *Physical Review Letters 100, 170506* (2008).

[20] E. Schrödinger. “Zur Theorie der Fall- und Steigversuche an Teilchen mit Brownscher Bewegung”. *Physikalische Zeitschrift 16, 289* (1915).

[21] F. Thiel, D. A. Kessler, and E. Barkai. “Spectral dimension controlling the decay of the quantum first-detection probability”. *Physical Review A 97, 062105* (2018).

[22] S. Dhar, S. Dasgupta, and A. Dhar. “Quantum time of arrival distribution in a simple lattice model”. *Journal of Physics A 48, 115304* (2015).

[23] H. Friedman, D. A. Kessler, and E. Barkai. “Quantum walks: The first detected passage time problem”. *Physical Review E 95, 032141* (2017).

[24] F. Thiel, E. Barkai, and D. A. Kessler. “First Detected Arrival of a Quantum Walker on an Infinite Line”. *Physical Review Letters 120, 040502* (2018).

[25] C. Cohen-Tannoudji, B. Diu, and F. Laloë. *Quantum Mechanics, Volume One*. John Wiley & Sons, 2005.

[26] R. Feynman, R. Leighton, and M. Sands. *The Feynman Lectures on Physics: Vol. III, the New Millennium Edition*. Basic Books, New York, 2010.

[27] M. Abramowitz and I. A. Stegun. *Handbook of Mathematical Functions with Formulas, Graphs and Mathematical Tables, Tenth Printing*. United States Department of Commerce, National Bureau of Standards, 1972.

[28] S. Elaydi. *An Introduction to Difference Equations, Third Edition*. Springer Science+Business Media, 2005.

[29] *numpy.linalg.eig - NumPy v1.19 Manual*. URL: `https://numpy.org/doc/stable/reference/generated/numpy.linalg.eig.html`. [accessed 05.07.2020].

[30] C. M. Bender and S. A. Orszag. *Advanced Mathematical Methods for Scientists and Engineers*. Springer Science+Business Media, 1999.

[31] *scipy.linalg.expm - SciPy v1.5.1 Reference Guide*. URL: `https://docs.scipy.org/doc/scipy/reference/generated/scipy.linalg.expm.html`. [accessed 08.07.2020].

[32] F. Thiel and D. A. Kessler. “Non-Hermitian and Zeno limit of quantum systems under rapid measurements”. *Physical Review A 102, 012218* (2020).

Eigenständigkeitserklärung

Hiermit versichere ich, die eingereichte Bachelorarbeit selbständig verfasst und keine anderen als die von mir angegebenen Quellen und Hilfsmittel benutzt zu haben. Wörtlich oder inhaltlich verwendete Quellen wurden entsprechend den anerkannten Regeln wissenschaftlichen Arbeitens (lege artis) zitiert. Ich erkläre weiterhin, dass die vorliegende Arbeit noch nicht anderweitig als Bachelorarbeit eingereicht wurde.

Ort, Datum	Unterschrift